# Transforming Nanocrystals into Superhard Boron Carbide Nanostructures

Fernando Igoa Saldaña, Thomas Gaudisson, Sylvie Le Floch, Benoît Baptiste, Ludovic Delbes, Virgile Malarewicz, Olivier Beyssac, Keevin Béneut, Cristina Coelho Diogo, Christel Gervais, et al.

# Transforming Nanocrystals into Superhard Boron Carbide Nanostructures

*Fernando Igoa Saldaña,[1,2] Thomas Gaudisson,[3] Sylvie Le Floch,[3] Benoît Baptiste,[2] Ludovic Delbes,[2] Virgile Malarewicz,[2] Olivier Beyssac,[2] Keevin Béneut,[2] Cristina Coelho Diogo,[4] Christel Gervais,[1] Gwenaëlle Rousse,[5] Karsten Rasim,[6] Yuri Grin,[6] Alexandre Maître,[7] Yann Le Godec[2,]* and David Portehault[1,]**

[1] Sorbonne Université, CNRS, Laboratoire de Chimie de la Matière Condensée de Paris (CMCP), 4 place Jussieu, F-75005, Paris, France

[2] Sorbonne Université, CNRS, MNHN, IRD, Institut de Minéralogie, de Physique des Matériaux et de Cosmochimie (IMPMC), 4 place Jussieu, F-75005, Paris, France

[3] Institut Lumière Matière, Université Lyon 1-CNRS, UMR 5306, Université de Lyon, 69622 Villeurbanne, France

[4] Sorbonne Université, CNRS, FCMat Fédération de Chimie et Matériaux de Paris Centre, FR2482, Paris, France

[5] Collège de France, Sorbonne Université, Chimie du Solide et de l'Energie (CSE), 75231 Paris Cedex 05, France

[6] Max-Planck-Institut für Chemische Physik fester Stoffe, Chemische Metallkunde, 01187 Dresden, Germany

[7] Institut de Recherche sur les Céramiques (IRCER), Centre Européen de la Céramique, 87068, Limoges, France

**ABSTRACT.** Boron carbide ($B_{4+\delta}C$) possesses a large potential as structural material owing to its lightness, refractory character and outstanding mechanical properties. However, its large-scale industrialization is set back by its tendency to amorphize when subjected to an external stress. In the present work, we design a path towards nanostructured boron carbide with greatly enhanced hardness and resistance to amorphization. The reaction pathway consists of triggering an isomorphic transformation of covalent nanocrystals of $Na_{1-x}B_{5-x}C_{1+x}$ ($x = 0.18$) produced in molten salts. The resulting 10 nm $B_{4.1}C$ nanocrystals exhibit a four-fold decrease of size compared to previous works. Solid-state $^{11}B$ and $^{13}C$ NMR coupled to DFT reveal that the boron carbide nanocrystals are made of a complex mixture of atomic configurations, which are located at the covalent structural chains between $B_{11}C$ icosahedral building units. These nanocrystals are combined with a spark plasma sintering-derived method operated at high pressure. This yields full densification while maintaining particle size. The nanoscaled grains and high density of grain boundaries provide the resulting nanostructured bodies with significantly enhanced hardness and resistance to amorphization, thus delivering a superhard material.

**KEYWORDS.** boron carbide, nanocrystals, hardness, spark plasma sintering, high pressure, molten salts.

## INTRODUCTION

Boron carbide ($B_{4+\delta}C$, with $-0.2 < \delta < 6.1$) [1] exhibits an attractive combination of low density (2.52 $g \cdot cm^{-3}$),[2] high melting point (2720 °C),[3] elevated elastic modulus (448 GPa),[4] incompressibility (adiabatic bulk modulus of 241 GPa),[5] and chemical inertness,[6] which make it one of the most performing refractory compounds.[7,8] Yet, its hardness is well below diamond and it does not exceed the hardness threshold for superhard materials (40 GPa) in its polycrystalline form. It is also subject to mechanical failure under stress,[9] including softening and fracture that are often ascribed to local amorphization.[10,11] This behavior strongly limits the range of applications of boron carbide.

We demonstrate herein how to overcome the current limitations of boron carbide as structural material by combining molten salts-mediated colloidal synthesis, nanocrystals transformation, and high-pressure flash sintering.

Boron carbide is built from covalently interconnected boron-based icosahedra as structural motifs. Each icosahedron contains polar (superindex *p*) and equatorial (superindex *e*) sites (**Figure 1a**). Every atom in a polar site links to another polar site of a neighboring icosahedron, while equatorial atoms bond to chains of ideally three atoms CBC. In the most widely accepted B-C phase diagram (**Figure 1b)**,[12] the boron carbide structure accommodates between 9 ($B_{10.1}C$) and 21 at. % ($B_{3.8}C$) of carbon.[1] The most common occurrence is 20 at. % C ($B_4C$). It should be ideally built from solely $B_{11}C^p$ clusters and CBC chains (($B_{11}C^p$)CBC structure), but this configuration is encountered together with different local arrangements, most notably at the three-atom chains.[13]

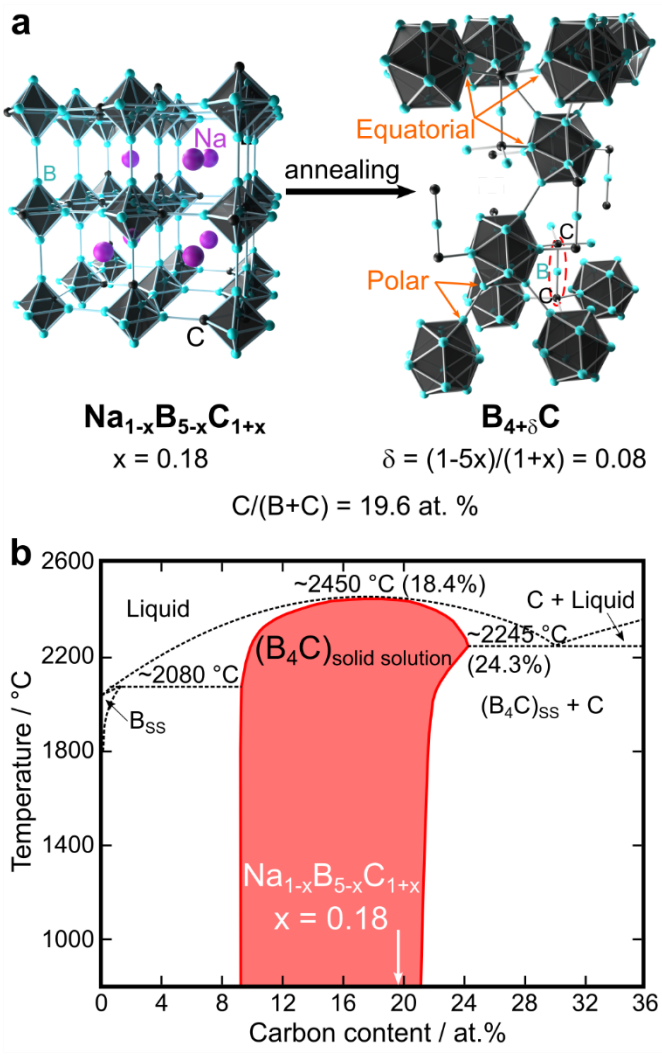


**Figure 1. Compositions and ideal structures of boron carbide and precursor sodium borocarbide. (a)** Scheme of the chemical pathway towards boron carbide nanocrystals, relying on the transformation of $Na_{1-x}B_{5-x}C_{1+x}$ into $B_{4+\delta}C$. In the $B_{4+\delta}C$ structure (rhombohedral $R\bar{3}m$ space group), CBC chains are highlighted in red and the polar/equatorial positions marked with arrows. From the boron-to-carbon ratio, the composition of the precursor sodium borocarbide is located within the homogeneity range of boron carbide in the (**b**) B-C phase diagram.[1] "SS" indices stand for "solid solution".

The hardness and resistance to amorphization of $B_{4+\delta}C$ have been previously enhanced by grain-boundary strengthening,[14] where grain boundaries pine the dislocations and impede their propagation. Decreasing the grain size down to the nanometric range limits the amount of

dislocations that can accumulate in a single grain and increases the density of grain boundaries. Therefore, the density of dislocations is decreased and their movement is restrained, thus hindering the onset of plasticity, of amorphization, and increasing the yield strength. This phenomenon, known as the Hall-Petch effect and observed for various materials, is typically optimized for grains of 5 - 50 nm,[15,16] but previous attempts for boron carbide were performed for particles at least an order of magnitude larger. This calls for the synthesis of sub-50 nm boron carbide nanocrystals and their compaction into dense bodies without grain growth, two currently unmatched objectives.

Carbothermal reduction is the most usual method to synthesize boron carbide,[17–19] but it does not yield microstructural control. Liquid-phase processes, like the sol-gel process, have enabled better morphological control down to the 40-90 nm range,[20] which is far from optimal to favor Hall-Petch strengthening. The difficulty to control the size of nanoparticles of boron carbide is intrinsic to its strong covalence, which requests high temperatures for crystallization and densification of powders.[21] Indeed, as for synthesis of small nano-objects, densification of boron carbide with limited grain growth remains a challenge. Sintering additives lower the densification temperature, but are detrimental to chemical stability and mechanical performances.[22] Spark plasma sintering using pulsed currents, usually at moderate pressures below 0.2 GPa, on one side, and high-pressure sintering on the other side, enable separately to limit grain growth and reach fully densified bodies (compaction above 99 %), but they have been applied only to micron-sized boron carbide grains.[23] Alternative crystallization and densification pathways are then mandatory to reach sub-50 nm boron carbide nanocrystals and to enable their densification.

To design boron carbide nanocrystals, we explore herein isomorphic transformation of precursor nanocrystals. Reacting nanocrystals by maintaining their shape and size is a well-

established approach to modify the composition or crystal structure of compounds bearing high ionicity or metallicity,[24] such as halides,[25] chalcogenides,[26] oxides,[27] and metal phosphides.[28] These transformations are much more difficult in compounds with predominant covalence because they require higher temperatures that are accompanied by morphological restructuration.[29] Boron carbide is prototypical of such solids. We have shown previously that sodium borocarbide $Na_{1-x}B_{5-x}C_{1+x}$ nanocrystals (**Figure 1a**) produced in molten salts might be efficient precursors of boron carbide nanocrystals through sodium elimination,[30] but only poor size control was achieved. Herein we show that by precisely tuning the composition of sodium borocarbide nanocrystals, we achieve composition and size control of ~10 nm boron carbide nanocrystals. We then go a step further, by triggering densification while maintaining the nanocrystal size. To achieve this behavior, we combine high pressures with spark plasma sintering (HP-SPS),[31] a recently issued method[32,33] that provides fast heating rates, short durations and moderate temperatures, but has never been applied to highly refractory boron carbide, a very hard-to-sinter material.

## RESULTS AND DISCUSSION

### $Na_{1-x}B_{5-x}C_{1+x}$ nanocrystals: Controlling the transformation to boron carbide through composition

The sodium borocarbide nanocrystals were synthesized by reacting sodium borohydride and polyethylene in molten sodium iodide at 900 °C. The original ratio of reactants[30] is set to a large excess of carbon to compensate for carbon losses during the synthesis (initial C:(B+C) = 56.1 at. % in contrast to 19.6 at. % in the resulting $Na_{1-x}B_{5-x}C_{1+x}$ (x = 0.18) nanocrystals and 16.7 at. % in the bulk compound). The retrieved sample is made of slightly elongated faceted nanoparticles

(**Figure S1a**) with a size distribution centred at 7 nm (**Figure 2**). High resolution transmission electron microscopy (HRTEM, **Figure S1a-b**) and selected area electron diffraction Debye rings (SAED, **Figure S1c**) confirm the expected $NaB_5C$ structure.[30] HRTEM also suggests the formation of single-crystalline domain particles that expose {100} facets. The particle size is consistent with the 5 nm diffraction domain size extracted from Le Bail refinement of the powder X-ray diffraction (XRD) pattern, which confirms the single crystal nature of the nanoparticles.[30]

The transformation of $Na_{1-x}B_{5-x}C_{1+x}$ nanocrystals into boron carbide ($B_{4+\delta}C$) occurs upon sodium evaporation during annealing at 1200 °C (**Figure 1a**), according to XRD (pattern recorded under argon in **Figure 3a**).[30] No trace of sodium was detected in the products by Energy Dispersive Spectroscopy (EDS), as discussed below in the processing section. TEM indicates evolution from a monomodal distribution of 5–7 nm sodium borocarbide nanocrystals (**Figure 2**) to a bimodal population upon boron carbide crystallization, with ~10 nm nanoparticles and more polydisperse objects up to 200 nm (**Figure S2a-b**). The former can be ascribed to direct transformation of the sodium borocarbide nanocrystals (Equation 1):

$$\frac{1}{1+x}\,Na_{1-x}B_{5-x}C_{1+x}(s) \rightarrow B_{4+\delta}C(s) + \frac{1-x}{1+x}\,Na(g) \qquad (1)$$

Equation (1) is valid if the C:(B+C) atomic ratio is maintained in the transformation from the sodium borocarbide to the boron carbide, hence $\delta = \frac{1-5x}{1+x} = 0.08 \approx 0.1$ for $x = 0.18$.

The larger objects suggest either uncontrolled growth of the particles, or an alternative boron carbide crystallization pathway. Indeed, the large excess of carbon source initially used could yield remaining free amorphous carbon with the sodium borocarbide nanocrystals. During annealing, carbon could react in turn with sodium borocarbide to form boron carbide, as a pathway

alternative to reaction (1). In agreement with this hypothesis, we observed that pristine boron carbide samples exhibit XRD patterns with a broad bump indicative of an amorphous component (**Figure 3a**) that evolves into boric acid $H_3BO_3$ upon exposure to air (**Figure 3a**). After boric acid removal and second exposure to air, the sample does not show new formation of boric acid (**Figure 3a**). Hence, the amorphous component and the derived boric acid do not arise from the reactivity of the boron carbide sample with air. Instead, the amorphous component forms during annealing. To ascertain the existence of a crystallization pathway parallel to the direct transformation of sodium borocarbide, due to remaining free carbon, we have screened the C:(B+C) ratio in the reaction mixture yielding sodium borocarbide from 56.1 to 44.4, 28.6 and 16.7 at. %. The resulting boron carbide samples exhibit narrowed size distribution (**Figure S2**), the narrowest one being obtained for initial 44.4 at. % (**Figures S2c-d** and **2a**), with particles of (10 ± 2) nm and a negligible proportion of larger objects compared to other reaction conditions. TEM and HRTEM (**Figure 2**) show preservation of the initial particle size. This indicates that by limiting excess carbon, one can trigger reaction (1) as the only pathway of boron carbide crystallization. This isomorphic crystallization enables size control. Note that some carbon excess is still needed to compensate for the low char yield of the polyethylene carbon source during the borocarbide synthesis.

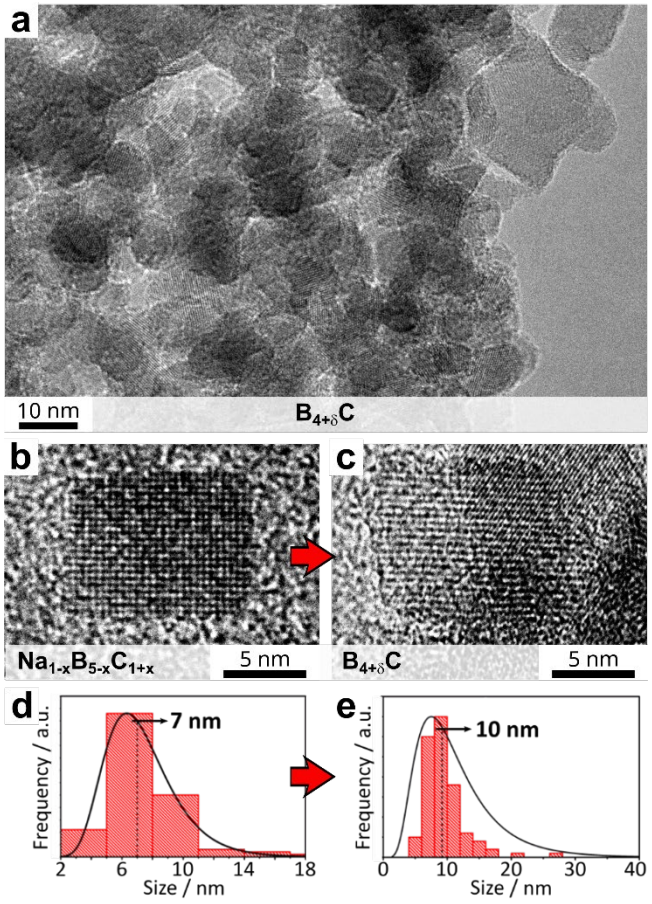


**Figure 2. Isomorphic conversion to size-controlled boron carbide nanocrystals with optimal C:(B+C) reagent ratio.** (a) TEM image of monodisperse boron carbide nanomaterial synthesized from $Na_{1-x}B_{5-x}C_{1+x}$ with C:(B+C) input ratio of 44.4 at. %. Comparison between (b) the initial $Na_{1-x}B_{5-x}C_{1+x}$ and (c) the final $B_{4.1}C$ nanostructures, illustrating successful size retention throughout the conversion. Size distribution from counting 100 particles fitted by a lognormal function of (d) the initial $Na_{1-x}B_{5-x}C_{1+x}$ and (e) the final $B_{4.1}C$ nanoparticles.

The average crystallite size of 10 nm for the sample corresponding to initial C:(B+C) ratio of 44.4 at. %. was retrieved from Le Bail refinement (**Figure 3, Table S1**). This value is consistent with TEM, confirms the retention of the original size of $Na_{1-x}B_{5-x}C_{1+x}$ nanocrystals, and further suggests that the boron carbide particles are single crystals. Successful size retention despite the high temperatures (1200 °C) involved is ascribed to the high covalency of both the reagent and

final product, which enables only short-range atomic movements during the transformation. Noteworthy, the particle size evaluated by TEM and XRD coincides with the theoretical optimum for Hall-Petch strengthening. No other synthesis process has delivered boron carbide particles smaller than 40 nm (**Table S2**). The lattice parameters retrieved from Le Bail refinement (**Figure 3, Table S1**, $a = b = 5.6012(2)$ Å, $c = 12.0792(3)$ Å) can be correlated by the Vegard's law (**Figure 3b** inset)[1] to a $B_{4.1}C$ stoichiometry (C:(B+C) = 19.6 at. %), fully consistent with retention of the C:(B+C) ratio of 19.6 at. % in the precursor borocarbide nanocrystals (**Figure 1**). The sample is named **nano-$B_{4.1}C$** hereafter.

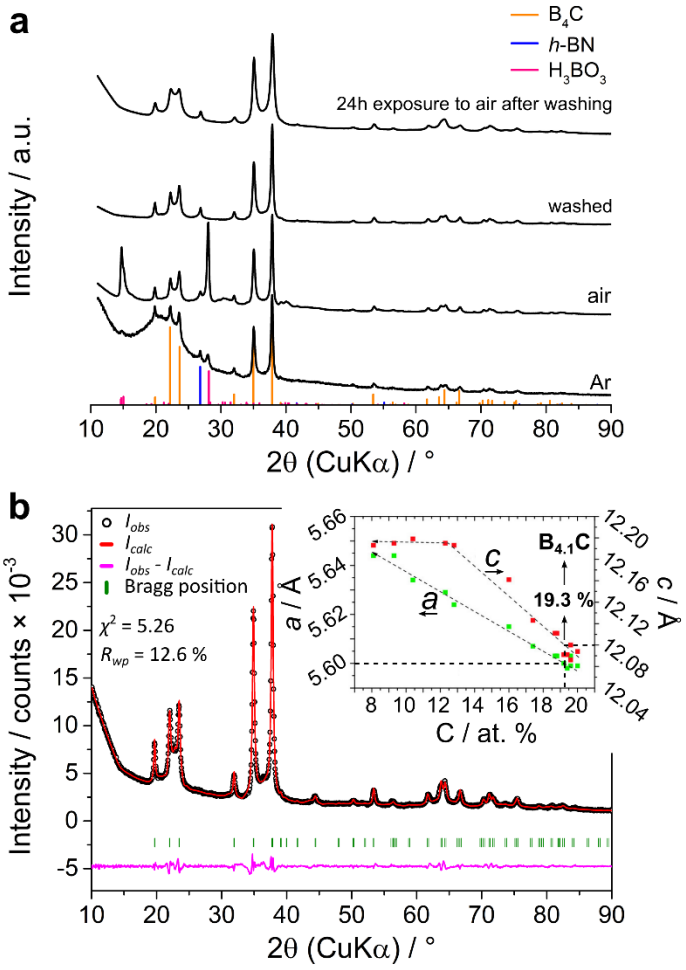


**Figure 3. Crystal structure and composition of size-controlled boron carbide nanocrystals.** (a) Powder XRD patterns of boron carbide powders obtained from calcination of $Na_{1-x}B_{5-x}C_{1+x}$

nanocrystals synthesized with initial C:(B+C) = 56.1 at. %. The patterns have been recorded under different conditions: argon atmosphere, air exposure, subsequent washing with methanol followed by drying, and then re-exposure during 24 h. The initial sample measured under argon already shows some diffraction peaks of $H_3BO_3$, which we ascribe to contamination of the sample with air leaking into the sample holder during XRD acquisition. (b) Le Bail refinement of the boron carbide product (**nano-$B_{4.1}C$**) obtained by conversion of $Na_{1-x}B_{5-x}C_{1+x}$ nanocrystals for C:(B+C) input ratio of 44.4 at. %. Inset: Vegard's law relationship between lattice parameters and the carbon content of boron carbide, with data obtained from reference [1]. The interpolation from the refined lattice parameters yields a $B_{4.1}C$ stoichiometry (19.3 % C *at*.).

**Local structure of size-controlled boron carbide nanocrystals**

Because the mechanical properties of boron carbide are linked to the local structure, and especially to the actual configuration of ideal inter-icosahedra chains,[34,35]we have delved into a precise investigation of the local structure of the boron carbide nanocrystals. Experimentally achieved boron carbide cannot be described by sole $(B_{11}C^p)$CBC units (**Figure 1a**).[1] Local defects, notably within the linear C-B-C chains, are a common occurrence. Rasim and collaborators identified experimentally at least five different local arrangements in the chain region for bulk boron carbide.[13] DFT calculations confirmed the observations, highlighting preferential configurations at lower energies with respect to standard CBC chains by ~ 1 eV/group.[13] We have then used $^{11}B$ and $^{13}C$ solid-state nuclear magnetic resonance (SS-NMR) to probe the local structure of the atomic chains in the as-synthesized boron carbide nanocrystals. $^{13}C$-SS-NMR measurements were performed on an isotopically enriched sample. To do so, we prepared a $Na_{1-x}B_{5-x}C_{1+x}$ precursor from $^{13}C$-enriched polyethylene, which was then calcined towards $^{13}C$-enriched boron carbide. All NMR spectra shown herein correspond to the $^{13}C$-enriched sample, including $^{11}B$-SS-NMR spectra. The experimental data (**Figure 4**) were interpreted thanks to DFT calculations of the NMR spectra, according to several structural models. Two initial models were considered for the average structure: $(B_{11}C^p)$CBC (**Figure 4a**) and $(B_{11}C^e)$CBC (**Figure 4b**) ($C^p$ and $C^e$ stand for the

icosahedral carbon atom in polar and equatorial positions, respectively). The experimental $^{11}$B-SS-NMR spectra recorded for the **nano-$B_{4.1}$C** sample and for a bulk $B_4C$ reference are depicted in **Figure 4c** with the corresponding simulated spectra. Similarly, $^{13}$C-SS-NMR spectra are shown in **Figure 4d** (without the bulk reference, as it was not $^{13}$C-enriched). Both ($B_{11}C^p$)CBC and ($B_{11}C^e$)CBC models fit the major signals of the $^{11}$B-SS-NMR spectra, but ($B_{11}C^e$)CBC fails to account for the $^{13}$C-SS-NMR results, as it predicts an extra signal at ~ 20 ppm, not observed experimentally. ($B_{11}C^p$)CBC fits better the $^{13}$C-SS-NMR spectrum and then is ascribed to the average structure. However, weak additional signals in the $^{11}$B and the $^{13}$C spectra are discerned (arrows in **Figure 4c-d** and **Figure 5**), similar to those reported for amorphous-$B_{2.5}C$.[36] The ($B_{11}C^p$)CBC model does not account for these contributions, which are then assigned to atomic configurations that deviate from the ideal model. We embarked in the identification of these features by considering alternative structural models.

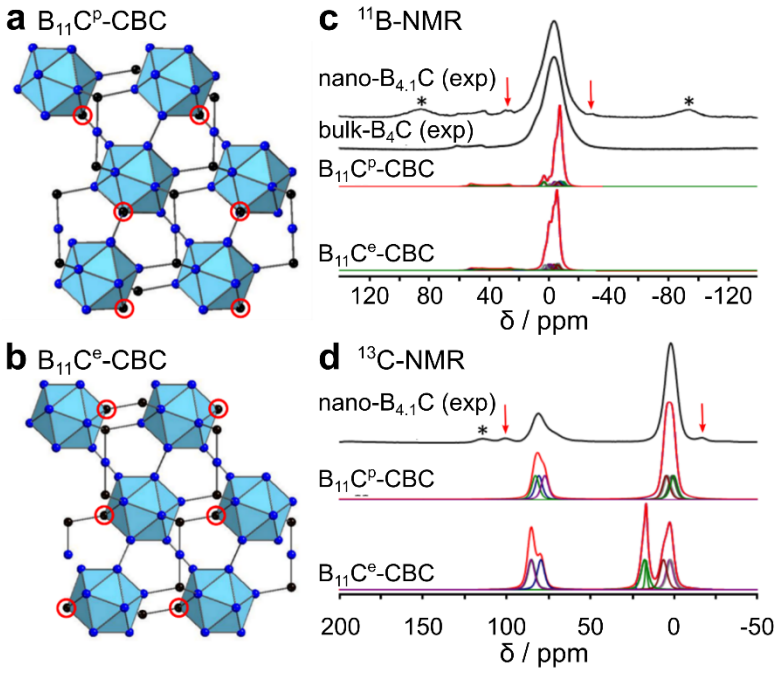


**Figure 4. SS-NMR study of the icosahedral B11C clusters of boron carbide nanocrystals.** Model structures are depicted for the **(a)** ($B_{11}C^p$)CBC (also displayed in **Figure 5**) and **(b)**

($B_{11}C^e$)CBC models, where the icosahedral C atoms in either the polar ($C^p$) or equatorial ($C^e$) positions are marked in red circles. Corresponding experimental and calculated $^{11}B$ and $^{13}C$ SS-NMR spectra are displayed in **(c)** and **(d)**, respectively. Additional signals not ascribed to the average structure are marked with red arrows and spinning side bands with an *.

Out of the 15 energetically favorable configurations that were evaluated for the chains,[13] two of them reproduced the additional signals in the NMR spectra: the rhombi-like BBBB (**Figure 5** and **Figure S3**) cluster and the linear chain CBC-B (**Figure 5** and **Figure S3**). These groups are also the two most stable configurations according to DFT calculations.[13] For comparison, some consistent features are also observed for a CBBB-B model with two additional boron atoms in the chain center and an additional boron along the chain (**Figure S3**), even if calculated $^{13}C$ signals around 50 ppm are not observed experimentally. As this model is less favorable energetically than the previous BBBB and CBC-C ones, it is not considered further. Other low energy defects[13] show weaker agreement with experimental data (**Figure S4**), especially for the $^{13}C$ spectra.

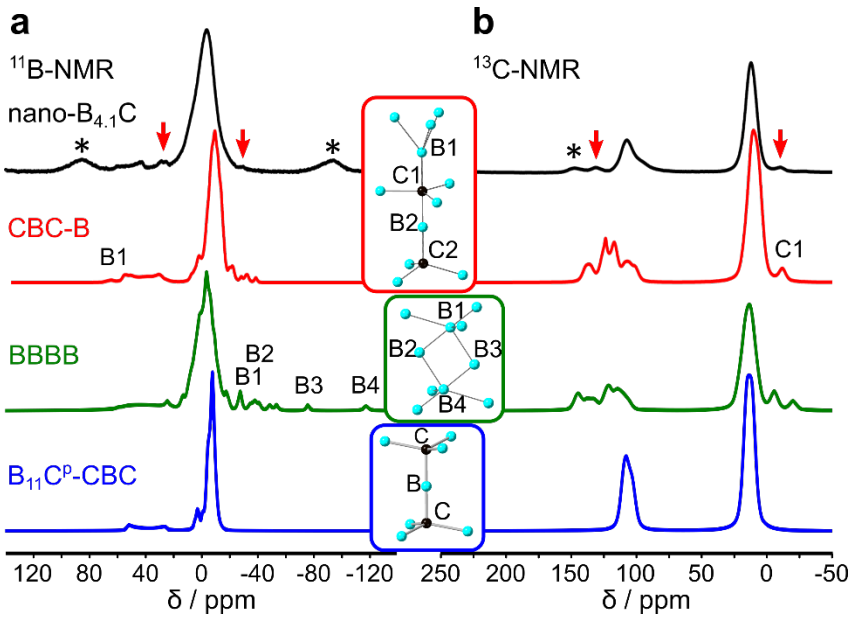


**Figure 5**. **SS-NMR study of the atomic arrangement at the chain sites of boron carbide nanocrystals.** (a) $^{11}$B-SS-NMR and (b) $^{13}$C-SS-NMR. In (a) and (b), the experimental spectra (nano-$B_{4.1}C$), and the DFT-simulated spectra for standard CBC chains ($(B_{11}C^{p})CBC$), BBBB clusters and CBC-B chains are stacked. Red arrows indicate the experimental contributions that are not accounted for by the CBC model but are consistent with BBBB and CBC-B configurations. spinning side bands are marked with an *. Middle insets: structural model of the chain geometry variations use for DFT simulation of the NMR spectra. Assignment of the most prominent features in the calculated spectra is given in **Figure S3**.

Most notably, the BBBB model reproduces all the observed signals while presenting certain not observed signals at 63 and -25 ppm in the $^{11}$B-NMR spectrum. On the other hand, the CBC-B motifs reproduced very well the $^{13}$C-NMR and the additional signal of the $^{11}$B-NMR at -25 ppm, although it does not show the contributions at 20 ppm. This suggests that a combination of the three environments CBC, BBBB and CBC-B could reproduce the overall NMR profile and is then representative of the local structure of boron carbide nanocrystals. Note that the local structure we describe herein corresponds to boron carbide nanocrystals derived from a specific conversion of precursor sodium borocarbide nanocrystals. Despite this process being very different

from more classical solid-state methods that yield bulk boron carbide, the chain configurations we detect are among those predicted as the most stable in bulk boron carbide.[13]

**Processing of boron carbide nanocrystals**

Once the purity, stoichiometry and size-control of the boron carbide nanocrystals were optimized, we sintered the powder to produce a dense monolith while maintaining grain size. This was performed in a prototype Paris-Edinburgh press coupled to a spark plasma device (**Figure S5**), at 5 GPa.[31,37] Here, contrary to conventional spark plasma sintering where the electrical current used for heating passes through the sample for localized heating and sintering, it goes through the outer graphite oven, separated from the sample by an insulating *h*-BN capsule, so that carbon cannot migrate from the oven to the sample. A fast heating ramp of 200 °C·min$^{-1}$ and a dwell time of 5 min were used. A slow cooling rate of 50 °C·min$^{-1}$ was applied down to 600 °C before abrupt temperature quenching to prevent the appearance of dislocations.[38,39] Two dwell temperatures were studied: 2100 °C and 2300 °C. The respective recovered densified monoliths are named **nano-$B_{4.1}C$-2100** and **nano-$B_{4.1}C$-2300**.

The power, resistance and anvils displacements were recorded throughout the procedure in order to understand the sintering process (**Figure S6**).[40] At least one major event occurs at 2000 °C, where the displacement transiently accelerates and the resistance abruptly decreases. This event lasts about 5 min and stops before the end of the temperature plateau, thus suggesting completion of the sintering. As expected, a sharp peak in the displacement speed curve appears when the heating slope changes from the ramp to the dwell step. Further spikes in the resistance curve can be ascribed to non-optimized contacts in the setup assembly.

The densities of the recovered monoliths measured by the Archimedes method are (97 ± 5) % and (99 ± 4) % for **nano-$B_{4.1}C$-2100** and **nano-$B_{4.1}C$-2300**, respectively. Scanning electron microscopy (SEM) for the **nano-$B_{4.1}C$-2300** surface confirm the poreless structure (**Figure S7**a). EDS coupled to SEM show that the nanostructured monoliths do not contain sodium (**Figure S7**b). Because sintering is performed in close-system conditions, the $B_{4.1}C$ nanocrystals obtained by annealing the sodium boron carbide nanocrystals were also exempt of sodium and Na was completely evaporated during annealing. XRD (**Figure 6**) performed on the sintered bodies detects *h*-BN impurities, coming from the sintering *h*-BN capsule. This is not threatening the mechanical properties, as boron nitride is located only at the periphery of the monolith, in the superficial part in contact with the capsule, as confirmed below by Raman microscopy. Le Bail analysis of the XRD patterns for both samples yields an average crystallite sizes of 16 and 21 nm for **nano-$B_{4.1}C$-2100** and **nano-$B_{4.1}C$-2300**, respectively (**Tables S3** and **S4**). Williamson-Hall plots[41] (**Figure S8**) for the **nano-$B_{4.1}C$** and the sintered **nano-$B_{4.1}C$-2300** samples confirm negligible strain in both cases and the assignment of XRD peak broadening to nanoscale crystallite size effect.

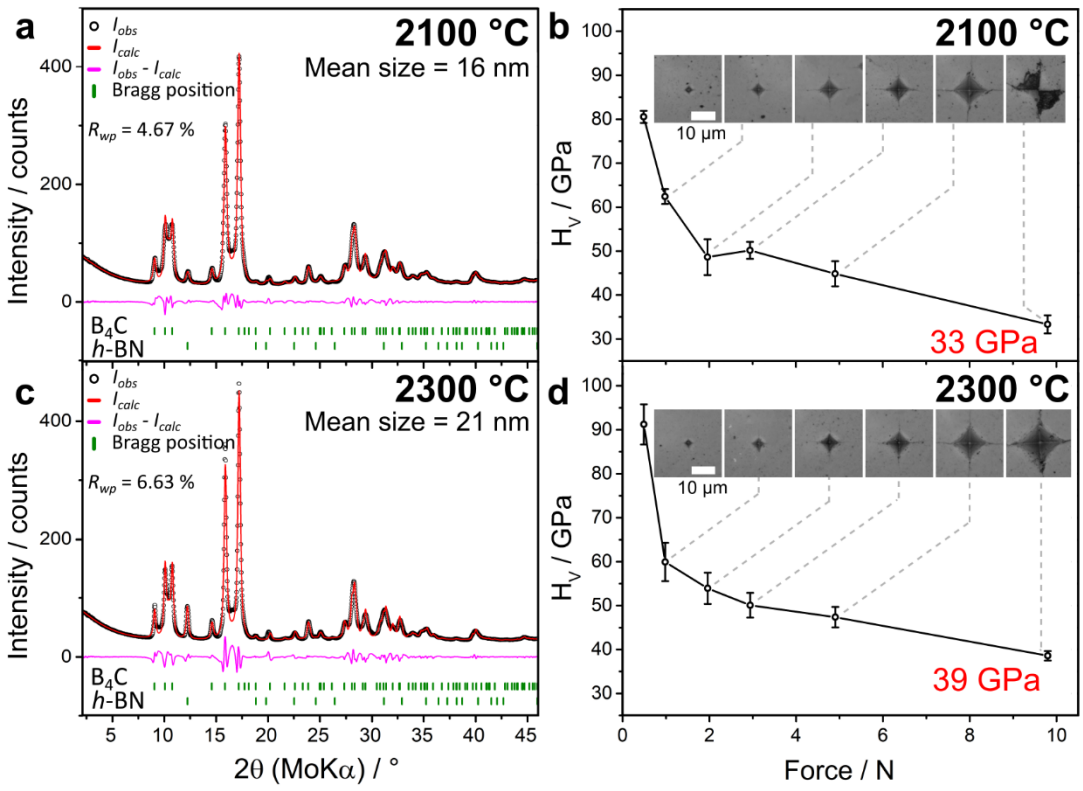


**Figure 6**. **Crystal structure and hardness of densified boron nanocrystals.** XRD patterns of the nano-$B_{4.1}C$ sintered bodies at 5 Gpa and (a) 2100 °C or (c) 2300 °C, with corresponding Le Bail refinements. Corresponding (b, d) Vicker's hardness curves in the 0.98 – 9.8 N load range.

## Hardness of boron carbide nanostructures

Vicker's microhardness curves were recorded for **nano-$B_{4.1}C$-2100** and **nano-$B_{4.1}C$-2300** bodies (**Figure 6**). We do not discuss further the low load domain, which is associated with large uncertainties for superhard materials.[42] Ideally, an asymptotic decay of the hardness should be observed down to a load-independent value. This is rarely the case in superhard (or close-to) materials, and instead, a load of 9.8 N in the Vicker's hardness ($VH_{9.8}$) is taken as reference, as per the ASTM-C1327 recommendations.[43] Both samples exhibit a high $HV_{9.8}$ hardness of (33 ± 2) and (39 ± 1) GPa respectively, the latter reaching the highest values reported for boron carbide

(**Table 1**). The higher hardness measured for the sample sintered at 2300 °C compared to the one obtained at 2100 °C is ascribed to its higher density, consistent with a poreless structure, as demonstrated above by density measurements and SEM.

We also evaluated the fracture toughness by using the extent of the cracks from the indentation vertexes. (1.29 ± 0.08) and (1.21 ± 0.06) $MPa \cdot m^{1/2}$ values are obtained at applied loads of 9.8 N for the 2100 and 2300 °C samples, respectively. Both values are smaller than those usually reported for boron carbide (2.5 – 3.0 $MPa \cdot m^{1/2}$), which is in line with the higher hardness, as harder materials tend to be more fragile, as particularly observed for boron carbide.[44] Although more thorough screening of sintering conditions could further improve hardness and fracture toughness, the values we report are already very high.

**Table 1**. Literature Vicker's hardness and Berkovich's nanohardness for boron carbide sample along with the main sample characteristics, as compared to the values reported in the present work.

| Grain size (nm) | Density (%)[a] | $VH_{9.8}$ (GPa) | Reference | Densification method |
|---|---|---|---|---|
| 21 | 99 | 39 ± 1 | This work | HP-SPS 5 GPa / 2300 °C |
| 16 | 97 | 33 ± 2 | This work | HP-SPS 5 GPa / 2100 °C |
| 2350 | 99.7 | 39 ± 1 | [39] | Hot-pressing 4.5 GPa / 1500 °C |
| 690 | 100 | 34 ± 2 | [44] | SPS 75 MPa / 1700 °C |
| 130 | 97 | 33 ± 3 | [23] | SPS 75 MPa / 1550 °C |
| 300 | 99.2 | 32 ± 1 | [14] | SPS 75 MPa / 2150 °C |
| 180 | 97.5 | 31 ± 3 | [23] | SPS 75 MPa / 1600 °C |
| 27700 | Not reported | 30 ± 2 | [45] | SPS 13.8 MPa / 2200 °C |
| 100 | 94.6 | 23 ± 3 | [23] | SPS 75 MPa / 1600 °C |
| 5000 – 10000 | 99 | 20 ± 2 | This work | HP-SPS 5 GPa / 2300 °C |
| **Grain size (nm)** | **Density (%)** | **$BH_{500}$ (GPa)** | **Reference** | |
| 21 | 99 | 43 ± 2 | This work | HP-SPS 5 GPa / 2300 °C |
| Single crystal[b] | 100 | 41.5 ± 1 | [46] | Floating zone crystal growth |
| Single crystal[c] | 100 | 40.5 ± 1 | [46] | |
| 5000 | 99.6 | 39 ± 2 | [47] | Hot-pressing (conditions not reported) |
| 40 – 150 | 92.8 | 20.5 ± 1.0 | [48] | Hot-pressing 980 GPa / 1600 °C |

[a] Density shown as percentage of the crystallographic density. [b] Measurement performed over the (0001) facet. [c] Measurement performed over the $(10\bar{1}1)$ facet.

For comparison, we produced a reference sample by sintering a commercial boron carbide powder with particle size ranging from 5 to 10 μm (named **micro-$B_4C$**), as confirmed by XRD and SEM-EDS (not shown). The sample was sintered under the same conditions as the **nano-$B_{4.1}C$-2300** sample. We measured an $HV_{9.8}$ hardness of (20 ± 2) GPa for the reference sample made of microscale particles, hence hardness much smaller than for the nanostructured nano-$B_{4.1}C$ samples (39 GPa). Therefore, nanostructuration yields a 95 % strengthening. This is in agreement with the extent of the Hall-Petch effect observed previously for other superhard materials, like cubic boron nitride, for which a polycrystalline sample is strengthened from an $HV_{9.8}$ of 45 GPa with micron-size grains to 85 GPa with nanodomains, that is a 89 % increase.[49] Similarly, 10-20 nm diamond samples showed a Knoop hardness ($H_K$) of up to 140 GPa, 100 % higher than its polycristalline counterpart ($H_K$ of 70 GPa maximum).[50] To further assess the intrinsic properties of sintered boron carbide, the Berkovich's nanohardness (BH) was also measured, by focusing on the most promising **nano-$B_{4.1}C$-2300** sample. With BH nanohardness measurements, the indentation tip leaves indents with lateral dimensions of ca. 500 nm, as opposed to 20 – 30 μm for Vicker's microhardness. As a consequence, nanohardness measurements are less sensitive to bulk effects like residual porosity, which may result from imperfect sintering, so that BH nanohardness is a better probe for the intrinsic mechanical properties and for potential nanostructuration effects. For a reference load of 500 mN, the measured $BH_{500}$ hardness goes as high as (43 ± 2) GPa. While the maximum Vicker's hardness achieved in this work has already been achieved by Liu and collaborators with samples of higher relative density,[39] the Berkovich's hardness is instead above values previously reported for boron carbide sintered compacts nor for boron carbide single crystals (**Table 1**), which highlights the key role of the nanostructure on enhancing hardness. The

resulting sintered boron carbide powders surpass the 40 GPa threshold to be ranked among superhard materials (**Table 1**). Liu et al.[39] showed how going from 99 to 99.7 % of density boosts the hardness by 20 %. This means that fine tuning sintering conditions of the boron carbide nanocrystals described herein to slightly increase the relative density may result in even higher hardness values, although it is outside the scope of this work, which demonstrates a leap in mechanical properties by designing nanostructures.

**Amorphization under load of boron carbide nanostructures**

The two limitations of boron carbide for mechanical applications are its limited hardness and its tendency to become amorphous under load. We have shown in the previous section that nanostructuration enables to bypass the first limitation. We have then addressed the amorphization behavior by using Raman microscopy as a probe to detect the amorphous phase.[48,51] The most promising sample **nano-$B_{4.1}C$-2300** and the reference microstructured boron carbide (**micro-$B_4C$**) were selected for this study. Raman spectra (**Figure 7**) were recorded in pristine regions and in areas indented at 9.8 N for microhardness measurements (**Figure 7c-e**). While prominent broad amorphization bands are observed above 1200 $cm^{-1}$ [48,51] in the indented region for the reference-$B_4C$, no major amorphization can be detected for **nano-$B_{4.1}C$-2300**. Note that the Raman spectrum of the nanostructured sample also confirmed the absence of graphite or hexagonal boron nitride in the core of the monolith, as the corresponding bands at ~1350 $cm^{-1}$ (graphite D band and *h*-BN $E_{2g}$ band) and ~1580 $cm^{-1}$ (graphite G band) are absent.[52]

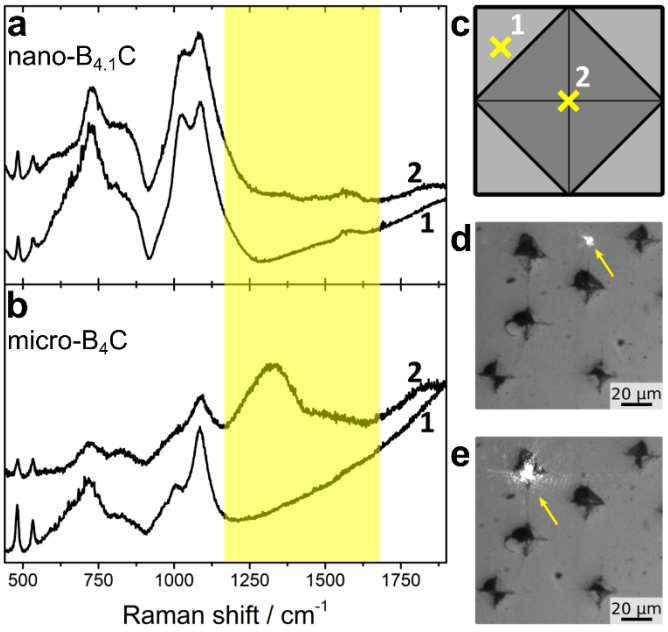


**Figure 7**. **Resistance to amorphization.** Raman spectra in pristine (1) and indented with a load of 9.8 N (2) zones for nano-$B_{4.1}C$ **(a)** and for the reference-$B_{4.1}C$ **(b)**, both sintered at 2300 °C and 5 GPa. **(c)** Indentation scheme and selected spots for acquiring Raman spectra. The actual probed spots are exemplified in **(d)** for the pristine region and **(e)** for the indented region, showing in the latter the imprecision and lack of resolution of the targeted position.

To probe the spatial distribution of the amorphized areas, we have performed Raman mapping with a 2.2×2.2 $\mu m^2$ spatial resolution for different loads. Quantitative information was obtained by Gaussian deconvolution on each Raman spectrum. The area of the peaks associated to the amorphized phase ($A_{am}$) were then evaluated with respect to the crystalline $B_{4.1}C$ Raman bands area ($A_{cr}$) to extract the relative amorphous peak area $A_{am,rel} = A_{am.}/(A_{am.} + A_{cr})$. $A_{am.}$ bands are defined as those between 1170 $cm^{-1}$ and 1670 $cm^{-1}$, while $A_{cr}$ bands are those between 450 $cm^{-1}$ and 1160 $cm^{-1}$ (**Figure 7**). The corresponding maps are displayed in **Figure 8**. Although a certain degree of amorphization occurs at the indents of the nanostructured body, it is significantly less than for the reference microstructured sample, with $A_{am,rel}$ reaching maximum values of 40 % and 100 % at 9.8 N for **nano-$B_{4.1}C$-2300** and reference boron carbide, respectively. Therefore,

nanostructuration not only significantly increases hardness, it is also strongly limiting the detrimental tendency of boron carbide to amorphization, thus providing a promising route to develop mechanically performing ceramics.

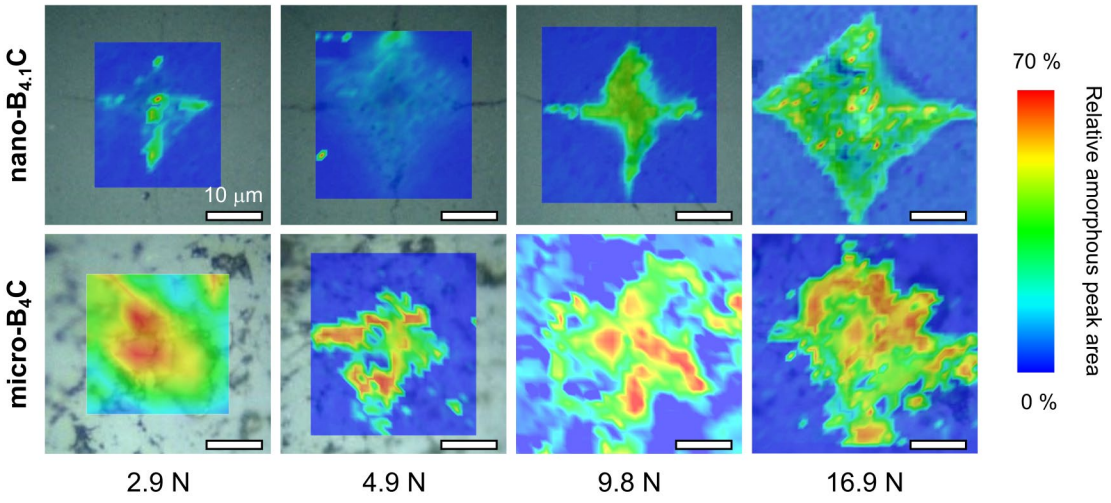


**Figure 8**. **Structural evolution under load of densified boron nanocrystals.** Raman mapping of the amorphous area at different indentation loads for nano-$B_{4.1}C$ **(a)** and for the reference micro-$B_4C$ **(b)**, both sintered at 2300 °C and 5 GPa. The intensity scale corresponds to the relative amorphous peak area $A_{am,rel}$. Scale bars correspond to 10 µm.

## CONCLUSION

By exploiting the conversion of sodium borocarbide nanocrystals produced in molten salts, we designed boron carbide nanocrystals with a narrow size distribution at 10 nm, hence a 4-fold decrease of the size compared to previous achievements. Therefore, we demonstrate that isomorphic transformation of nanocrystals can be achieved for highly covalent materials, provided that the reaction temperature is sufficient to trigger structural changes. By using this approach, we could elucidate the local structure of these nano-objects. While they are built mainly from traditionally considered carbon-boron-carbon covalent chains, they also contain additional atomic

arrangements consisting of four-fold boron clusters and linear carbon-boron-carbon-boron chains. By combining these nanocrystals with high-pressure spark plasma sintering, we reached fully densified nanostructured bodies with retained grain size, thus delivering strongly increased hardness, a superhard material, and high resistance against amorphization under load. All these features can be ascribed to grain-boundary strengthening. Therefore, we demonstrate that nanostructuration yields boron carbide-based materials with high potential in mechanical applications. This synthesis route towards boron carbide nanocrystals provides perspectives for the design of superhard materials, as one can capitalize on the well-furnished toolbox of colloidal synthesis in molten salts[53] to adjust the size and the deviation to stoichiometry of the precursor sodium borocarbide nanocrystals, and then assess the role of size and composition on the mechanical properties of nanostructured boron carbide.

## MATERIALS AND METHODS

All reagents were stored and handled in an argon-filled glove box. $Na_{1-x}B_{5-x}C_{1+x}$ nanocrystals were obtained from a modification of a protocol described elsewhere.[30] Briefly, the synthesis relies on the reaction between sodium borohydride and polyethylene in molten sodium iodide at 900 °C under argon. The nanocrystals are purified by cycles of redispersion-centrifugation in methanol (VWR Normapur grade). After drying, they are stored in an argon-filled glovebox. The boron-to-carbon ratio (B:C) in $Na_{1-x}B_{5-x}C_{1+x}$ ($x$ value) was screened by modifying the ratio between boron and carbon sources for B:C ratios of 5:6.4, 5:4, 5:2, 5:1 at. CORTECNET 99% $^{13}C$-enriched polyethylene was used for synthesizing $^{13}C$-enriched $Na_{1-x}B_{5-x}C_{1+x}$ and the resulting $^{13}C$-enriched

$B_{4+\delta}C$. Typically, 150 mg of $Na_{1-x}B_{5-x}C_{1+x}$ product was obtained per batch. A commercial $B_4C$ powder was used as reference (5 μm < particle size < 10 μm, 98 %, Sigma).

**Isomorphic synthesis of $B_{4+\delta}C$ nanocrystals:** The initial $Na_{1-x}B_{5-x}C_{1+x}$ powder was placed into an *h*-BN crucible inside an Ar-filled glove box and sealed with parafilm. The crucible was transferred to a previously Ar purged (for 1 h) horizontal tubular oven, which was then further purged with Ar flow for 1 hour before being heated under argon flow up to 1200 °C at a heating rate of 5 °C $min^{-1}$. Then the temperature was dwelled for 12 hours before stopping heating and letting the oven cool down naturally. The resulting powder was washed with methanol by cycles of centrifugation and redispersion until a conductivity of 4 $\mu S \cdot cm^{-1}$ in the supernatant was achieved. The sample was stored in air. The procedure was analogous for the different B:C ratios and for the $^{13}C$-enriched sample. A whole $Na_{1-x}B_{5-x}C_{1+x}$ batch (150 mg) was used per $B_{4+\delta}C$ synthesis.

**Spark-Plasma Sintering at high-pressure:** The produced boron carbide powders were densified by using a custom-made spark plasma sintering (SPS) equipment coupled to a Paris-Edinburgh press.[31,37] In an argon-filled glovebox, $B_{4+\delta}C$ powders were compacted and loaded into a Ø (3 mm outer, 2.5 mm inner) × H 3 mm *h*-BN capsule, which was assembled inside a conventional 10×6.6 mm baked pyrophyllite high-pressure set-up and then placed into a Paris-Edinburgh anvils assembly as described by Le Godec and co-workers.[54] The filled mass varied between 9 and 11 mg. Briefly, the set-up was compressed between two tungsten carbide conical anvils with a specially designed bottom part to improve mechanical strength and compression.[54,55] The high-resistivity graphite inside the assembly was used as heater by injecting controlled electrical current from the anvils through the assembly. Pulsed current was passed in patterns consisting of trains of

twelve 3.3 ms pulses with two of the same pulses as lap time in between trains. The temperature was monitored from a previous calibration to the delivered power. The samples were compressed at 5 GPa at a pressing ramp of 100 MPa $min^{-1}$ $s^{-1}$ in a four columns V4 Paris-Edinburgh press. Once the desired pressure was reached, the samples were heated to the targeted temperature using the following heating profile: heat at a rate of 200 °C $min^{-1}$ up to dwell temperature – hold for 5 min – cool at 50 °C $min^{-1}$ down to 600 °C – quench heating by shut off the power supply – release the pressure at 25 Mpa $min^{-1}$. The assemblies were then cut and opened under air and the products recovered for further analysis. A reference sintered sample was performed from a boron carbide powder purchased from Sigma (98% purity) with particle size ranging from 5 to 10 μm.

**Powder X-ray diffraction (XRD):** Powders produced at room-pressure were analyzed by powder XRD in a Bruker D8 Advance diffractometer in the Bragg-Brentano θ-θ geometry. The X-ray source consisted of a sealed Cu anode with emission lines sited at $K_{\alpha1}$ = 1.5406 Å, $K_{\alpha2}$ = 1.5443 Å, with an acceleration tension of 40 kV and a current of 30 mA. Diffracted intensity was detected using a LynxEye linear detector. Powder patterns were collected in the 2θ range 10-90° with a step of 0.0486° and 5 s $step^{-1}$. X-ray diffractograms of the pelletized compacts retrieved from high-pressure experiments were obtained from a Rigaku MM07HF diffractometer equipped with a microfocus Mo rotating anode ($K_{\alpha1}$ = 0.709319Å, $K_{\alpha2}$ = 0.713609 Å) and a RAXIS4++ image plate detector. The sample was mounted in the head of a rotating goniometer and a 15 min phi scan with angular amplitude of 40° and rotation speed of 20° $s^{-1}$ was performed. An $LaB_6$ NIST standard sample was measured in the same experimental conditions to calibrate the Fit2D program, the image processing software used to integrate the intensities around the Debye-Scherrer rings and to get the 1D patterns.[56] The reference crystallographic structures were taken from the ICSD database: $B_4C$ (ICSD #79958), $H_3BO_3$ (ICSD #24711) and *h*-BN (ICSD #241875). The powder

patterns were refined following the Le Bail algorithm, where the Bragg intensities are empirically adjusted and thus not calculated from structure factors.[57] Refinements were performed using the FullProf suite of programs.[58] For data recovered from the Bruker D8 Advance diffractometer, an $Al_2O_3$ NIST pattern was used to determine the instrumental function. For data recovered from the Rigaku MM07HF diffractometer, a $LaB_6$ NIST pattern was used for the same purposes.

**Transmission electron microscopy (TEM):** Transmission electron microscopy analyses were performed in a Tecnai Spirit 2 apparatus, equipped with a $LaB_6$ electron gun, operating at 120 kV. Samples were dispersed by sonication in ethanol and deposited on top of Cu grids covered with a carbon membrane.

**Solid-State Magic Angle Spinning – Nuclear Magnetic Resonance (SS–NMR):** Solid-state MAS NMR spectra were acquired on a Bruker AVANCE III 700 spectrometer (16.4 T) operating at $\nu_0$ = 224.68 and *176.01* MHz for $^{11}B$ and $^{13}C$, respectively, and using *a 3.2 mm Bruker probe*. Powder samples were transferred to $ZrO_2$ rotors and spun at a MAS rate of 20 kHz. Single pulse $^{13}C$ MAS NMR spectra were recorded with a recycle delay of 120 s while $^{11}B$ MAS NMR spectra were acquired using a spin-echo $\theta$-$\tau$-2$\theta$ pulse sequence with $\theta = 90°$, to overcome problems related to the probe signal. The $\tau$ delay (50 μs) was synchronized with the spinning frequency and recycle delay was set to 2 s. $^{13}C$ and $^{11}B$ chemical shifts were referenced to TMS and $BF_3{\cdot}Oet_2$, respectively.

**Nuclear Magnetic Resonance modelling – $B_{4+\delta}C$:** Two basic $B_4C$ models were obtained starting from the crystalline structure of $B_4C$ (**Figure 1a** and **Figure 4**): (i) (ICSD #79958) polar $(B_{11}C^p)$CBC model using a CBC chain and $B_{11}C$ icosahedra with the C atom in a polar site; (ii) equatorial $(B_{11}C^e)$CBC model using a CBC chain and $B_{11}C$ icosahedra with the C atom in an

equatorial site. In addition, more complex models proposed by K. Rasim et al.[13] on the basis of DFT calculations were also investigated. They are composed of 2×2×1 hexagonal supercells containing initially 180 atoms, which corresponds to 12 chain-icosahedron building blocks ($B_{12}$+CBC i.e. $B_{156}C_{24}$). In these models, one CBC chain motif is modified with different local atomic arrangements, whether the chain contains four atoms instead of three, or the boron atoms of the chain are located out of the three-fold axis, forming bent chains CBC or rhombi $CB_2C$. We investigated more specifically most energetically favourable structures (see schemes in **Figure 5**):[13] (iii) CBC-B with an additional boron atom on top of the chain; (iv) BBBB with two additional boron atoms in the center of the chain and no more carbon in this chain; and (v) CBBB-B with two additional boron atoms in the center chain and one boron above the chain, which leaves just one carbon. For comparison, we also investigated less energetically favourable models described in **Figure S4**. For all models from iii, changing the chain atomic arrangements modifies the electron filling of the valence states.[13] We ensured that the models used for DFT calculations were corresponding to the expected semiconducting behavior of boron carbide by adapting the boron-to-carbon stoichiometry , i.e. by adding carbon atoms until all valence states are filled, which does not necessarily renders the $B_{4.1}C$ empirical stoichiometry, but is still more representative of the actual behavior of boron carbide than a metallic behavior. These additional carbon atoms were introduced in the polar position of the icosahedra, because this allows for the best match with experimental NMR data (**Figure S4**). The NMR parameters were then calculated for all these models within Kohn-Sham DFT using the QUANTUM-ESPRESSO code.[59] The PBE generalized gradient approximation[60] was used and the valence electrons were described by norm conserving pseudopotentials[61] in the Kleinman Bylander form.[62] The shielding tensor was computed using the Gauge Including Projector Augmented Wave (GIPAW) approach,[63] which enables the

reproduction of the results of a fully converged all electron calculation. The isotropic chemical shift $\delta_{iso}$ is defined as $\delta_{iso} = -[\sigma - \sigma_{ref}]$ where $\sigma$ is the isotropic shielding and $\sigma_{ref}$ is the isotropic shielding of the same nucleus in a reference system. In the present case, the comparison between the experimental $\sigma_{iso}$ and calculated $\sigma_{iso}$ $^{11}B$ and $^{13}C$ chemical shift values for $B_2O_3$ (ICSD #16021) and amino acids[64] were used as previously described. The principal components $V_{xx}$, $V_{yy}$, and $V_{zz}$ of the electric field gradient (EFG) tensor were obtained by diagonalization of the calculated tensor giving access to the quadrupolar coupling constant $C_Q$ and the asymmetry parameter $\eta_Q$, which are defined as: $C_Q = eQV_{zz}/h$ and $\eta_Q = (V_{yy} - V_{xx})/V_{zz}$ ($e$ is the proton charge, $h$ is the Planck constant and $Q$ the quadrupole moment of the considered nucleus). The $Q$ value reported by Pyykkö[65] was used in the calculations for $^{11}B$ (40.59 mb). Calculated spectra were then plotted using the DMFit program.[66]

**Scanning electron microscopy (SEM) and Energy dispersive X-ray spectroscopy (EDS):** The scanning electron microscopy images were taken on a SEM-FEG HITACHI SU-70 microscope without any conductive deposition. EDS spectra were acquired with an electron accelerating voltage of 10 kV.

**Vicker's microhardness measurements:** For performing Vickers hardness characterization, the compressed pellets were first embedded in an acrylic resin of methyl methacrylate for polishing. The composite was thoroughly polished using SiC polishing paper up to grit sizes of P2000. Surface flatness was confirmed by optical microscopy. Vickers hardness measurements have been performed using a microhardness tester (Duramin-20, Struers) under the load from 0.49 to 19.6 N. At least ten indentations were performed for each data point to provide good statistics. The radial

cracks observed at the loads of 10 and 20 N allowed us to calculate the reliable load-independent value of fracture toughness by the method that was previously used for other superhard materials.[67]

**Berkovich's nanohardness measurements:** Berkovich nanohardness measurements were performed on the same samples used for Vicker's microhardness. An XP diamond nanoindenter (MTS Nano Instruments, Santa Clara, USA) was used under a 500 mN load. At least ten indentations were performed for each data point to provide good statistics.

**Density measurement:** The density of the sintered samples was measured using Archimedes method with distilled water as a liquid medium. The values for the relative densities were calculated assuming a theoretical density of $B_{4.1}C$, that is 2.52 g $cm^{-3}$.

**Raman spectroscopy and mapping:** Raman spectra of $Na_{1-x}B_{5-x}C_{1+x}$ powders were acquired on a Kaiser Optical System Raman Analyzer RX1 Microprobe with a 785 nm laser diode. Raman spectra of mechanically tested $B_{4+\delta}C$ samples were acquired using a Jobin-Yvon/Horiba HR-460 spectrometer equipped with a monochromator with 1500 grooves·$mm^{-1}$ and an Andor CCD. An Argon laser operating at 514.5 nm was focused on the sample with an optical lens and the backscattered Raman spectra in the Raman shift 470 – 1900 $cm^{-1}$ range were collected with a laser power of ~ 50 μW and averaged from 3 accumulations, each with a collection time of 300 s. Raman hyperspectral maps were recorded using a Renishaw InVia spectrometer equipped with a 532 nm Cobolt diode laser. The laser was focused on the sample using a DM2500 Leica microscope with a long working-distance 50× objective (NA = 0.55) to obtain a planar resolution of ~ 1 $\mu m^2$. The laser power at the sample surface was set at around 5 mW using neutral density filters to avoid damages due to laser-induced heating. The signal was filtered by edge filters and dispersed by a diffraction grating with 2400 grooves per mm and the signal was analyzed with a RENCAM

CCD (charge-coupled device) detector. The spectrometer was calibrated using a silicon standard. Spectra were collected using the software WIRE 4.4 provided by Renishaw. More details on hyperspectral mapping using such configuration may be found in ref [68].

## ASSOCIATED CONTENT

**Supporting Information**. The following data are available free of charge. Structural and morphological characterization of initial sodium borocarbide nanocrystals (Figure S1) and of derived boron carbide nanocrystals (Figures S2-S4, Table S1). Literature survey of achieved boron carbide particle sizes (Table S2). Densification of size-controlled boron carbide nanocrystals (Figures S5-S6, Tables S3-S8).

## AUTHOR INFORMATION


### Corresponding Authors

*To whom correspondence should be addressed: David Portehault, david.portehault@sorbonne-universite.fr, Yann Le Godec, yann.le_godec@sorbonne-universite.fr


### Author Contributions

FI, YLG and DP conceptualized the study. FI, YLG and DP acquired funding for the study. FI performed the synthesis, characterization, and processing work. CG performed the NMR work with CCD. CG led the NMR simulation work. TG and SLF contributed to the processing part. BB, LD, VM, OB and KB participated to structural characterization. AM performed the mechanical

studies. All authors contributed to data analysis. FI produced the first draft of the manuscript. The manuscript was written through contributions of all authors. All authors have given approval to the final version of the manuscript.

**Funding Sources**

The authors acknowledge the French Ministry for Research and the Doctoral School ED397 for funding of F.I.

**Notes**

The authors declare no competing financial interest

ACKNOWLEDGMENT

The authors acknowledge the French Ministry for Research and the Doctoral School ED397 for the Ph.D. fellowship of F.I. They also acknowledge the FCMat platform of Sorbonne Université for NMR measurements.

## REFERENCES


(1) Domnich, V.; Reynaud, S.; Haber, R. A.; Chhowalla, M. Boron Carbide: Structure, Properties, and Stability under Stress. *J. Am. Ceram. Soc.* **2011**, *94* (11), 3605–3628. https://doi.org/10.1111/j.1551-2916.2011.04865.x.

(2) Clark, H. K.; Hoard, J. L. The Crystal Structure of Boron Carbide. *J. Am. Chem. Soc.* **1943**, *65* (11), 2115–2119. https://doi.org/10.1021/ja01251a026.

(3) Mukhanov, V. A.; Sokolov, P. S.; Solozhenko, V. L. On Melting of B4C Boron Carbide under Pressure. *J. Superhard Mater. 2012 343* **2012**, *34* (3), 211–213. https://doi.org/10.3103/S1063457612030100.

(4) Ramana Murthy, S. Elastic Properties of Boron Carbide. *J. Mater. Sci. Lett.* **1985**, *4*, 603–605.

(5) Dodd, S. P.; Saunders, G. A.; James, B. Temperature and Pressure Dependences of the Elastic Properties of Ceramic Boron Carbide (B4C). *J. Mater. Sci.* **2002**, *37*, 2731–2736. https://doi.org/10.1007/BF01730603.

(6) Sezer, A. O.; Brand, J. I. Chemical Vapor Deposition of Boron Carbide. *Mater. Sci. Eng. B* **2001**, *79* (3), 191–202. https://doi.org/10.1016/S0921-5107(00)00538-9.

(7) Suri, A. K.; Subramanian, C.; Sonber, J. K.; R. Ch. Murthy, T. S. Synthesis and Consolidation of Boron Carbide: A Review. *Int. Mater. Rev.* **2013**, *55* (1), 4–40. https://doi.org/10.1179/095066009X12506721665211.

(8) May, P. W. The New Diamond Age? *Science.* **2008**, *319* (5869), 1490–1491. https://doi.org/doi/10.1126/science.1154949.

(9) Li, P.; Bu, Y.; Wang, L.; Wang, C.; Huang, J.; Tong, K.; Chen, Y.; He, J.; Zhao, Z.; Xu, B.; et al. In Situ Observation of Fracture along Twin Boundaries in Boron Carbide. *Adv. Mater.* **2023**, *35* (50), 1–7. https://doi.org/10.1002/adma.202204375.

(10) Mashimo, T.; Uchino, M. Heterogeneous Free-Surface Profile of B4C Polycrystal under Shock Compression. *J. Appl. Phys.* **1997**, *81*, 7064. https://doi.org/10.1063/1.365229.

(11) Chen, M.; Mccauley, J. W.; Hemker, K. J. Shock-Induced Localized Amorphization in Boron Carbide. *Science.* **2003**, *299*, 1563–1566.

(12) Beauvy, M. Stoichiometric Limits of Carbon-Rich Boron Carbide Phases. *J. Less-Common Met.* **1983**, *90*, 169–175.

(13) Rasim, K.; Ramlau, R.; Leithe-Jasper, A.; Mori, T.; Burkhardt, U.; Borrmann, H.; Schnelle, W.; Carbogno, C.; Scheffler, M.; Grin, Y. Local Atomic Arrangements and Band Structure of Boron Carbide. *Angew. Chemie Int. Ed.* **2018**, *130* (21), 6238–6243. https://doi.org/10.1002/anie.201800804.

(14) DeVries, M.; Pittari, J.; Subhash, G.; Mills, K.; Haines, C.; Zheng, J. Q.; Zok, F. Rate-

Dependent Mechanical Behavior and Amorphization of Ultrafine-Grained Boron Carbide. *J. Am. Ceram. Soc.* **2016**, *99* (10), 3398–3405. https://doi.org/10.1111/JACE.14324.

(15) Petch, N. J. The Cleavage Strength of Polycrystals. *J. Iron Steel Inst.* **1953**, *174*, 25–28.

(16) Hall, E. O. The Deformation and Ageing of Mild Steel: III Discussion of Results. *Proc. Phys. Soc. Sect. B* **1951**, *64* (9), 747–753. https://doi.org/10.1088/0370-1301/64/9/303.

(17) Alizadeh, A.; Taheri-Nassaj, E.; Ehsani, N.; Baharvandi, H. R. Production of Boron Carbide Powder by Carbothermic Reduction from Boron Oxide and Petroleum Coke or Carbon Active. *Adv. Appl. Ceram.* **2006**, *105* (6), 291–296. https://doi.org/10.1179/174367606X146685.

(18) Jung, C. H.; Lee, M. J.; Kim, C. J. Preparation of Carbon-Free B4C Powder from B2O3 Oxide by Carbothermal Reduction Process. *Mater. Lett.* **2004**, *58* (5), 609–614. https://doi.org/10.1016/S0167-577X(03)00579-2.

(19) Herth, S.; Joost, W. J.; Doremus, R. H.; Siegel, R. W. New Approach to the Synthesis of Nanocrystalline Boron Carbide. *J. Nanosci. Nanotechnol.* **2006**, *6* (4), 954–959. https://doi.org/10.1166/jnn.2006.186.

(20) Gu, Y.; Chen, L.; Qian, Y.; Zhang, W.; Ma, J. Synthesis of Nanocrystalline Boron Carbide via a Solvothermal Reduction of CCl4 in the Presence of Amorphous Boron Powder. *J. Am. Ceram. Soc.* **2005**, *88* (1), 225–227. https://doi.org/10.1111/j.1551-2916.2004.00023.x.

(21) Waller, P. J.; Gándara, F.; Yaghi, O. M. Chemistry of Covalent Organic Frameworks. *Acc. Chem. Res.* **2015**, *48* (12), 3053–3063. https://doi.org/10.1021/acs.accounts.5b00369.

(22) Matović, B.; Urbanovich, V.; Girman, V.; Lisnichuk, M.; Nikolić, D.; Erčić, J.; Cvijović-Alagić, I. Densification of Boron Carbide under High Pressure. *Mater. Lett.* **2022**, *314*. https://doi.org/10.1016/j.matlet.2022.131877.

(23) Moshtaghioun, B. M.; Ortiz, A. L.; Gómez-García, D.; Domínguez-Rodríguez, A. Densification of B4C Nanopowder with Nanograin Retention by Spark-Plasma Sintering. *J. Eur. Ceram. Soc.* **2015**, *35* (6), 1991–1998. https://doi.org/10.1016/j.jeurceramsoc.2014.12.021.

(24) Manna, L.; Cheon, J.; Schaak, R. E. Why Do We Care about Studying Transformations in Inorganic Nanocrystals? *Accounts of Chemical Research*. American Chemical Society April 6, 2021, pp 1543–1544. https://doi.org/10.1021/acs.accounts.1c00123.

(25) Toso, S.; Baranov, D.; Manna, L. Metamorphoses of Cesium Lead Halide Nanocrystals. *Acc. Chem. Res.* **2021**, *54* (3), 498–508. https://doi.org/10.1021/acs.accounts.0c00710.

(26) Schaak, R. E.; Steimle, B. C.; Fenton, J. L. Made-to-Order Heterostructured Nanoparticle Libraries. *Acc. Chem. Res.* **2020**, *53* (11), 2558–2568. https://doi.org/10.1021/acs.accounts.0c00520.

(27) Baktash, E.; Capitolis, J.; Tinat, L.; Larquet, C.; Chan Chang, T. H. C.; Gallet, J. J.; Bournel, F.; Sanchez, C.; Carenco, S.; Portehault, D. Different Reactivity of Rutile and Anatase TiO2

Nanoparticles: Synthesis and Surface States of Nanoparticles of Mixed-Valence Magnéli Oxides. *Chem. - A Eur. J.* **2019**, *25* (47), 11114–11120. https://doi.org/10.1002/chem.201901592.

(28) Carenco, S.; Portehault, D.; Boissière, C.; Mézailles, N.; Sanchez, C. 25th Anniversary Article: Exploring Nanoscaled Matter from Speciation to Phase Diagrams: Metal Phosphide Nanoparticles as a Case of Study. *Adv. Mater.* **2014**, *26* (3), 371–390. https://doi.org/10.1002/adma.201303198.

(29) Song, Y.; Gómez-Recio, I.; Ghoridi, A.; Igoa Saldaña, F.; Janisch, D.; Sassoye, C.; Dupuis, V.; Hrabovsky, D.; Ruiz-González, M. L.; González-Calbet, J. M.; et al. Heterostructured Cobalt Silicide Nanocrystals: Synthesis in Molten Salts, Ferromagnetism, and Electrocatalysis. *J. Am. Chem. Soc.* **2023**, *145* (35), 19207–19217. https://doi.org/10.1021/jacs.3c01110.

(30) Delacroix, S.; Igoa, F.; Song, Y.; Le Godec, Y.; Coelho-Diogo, C.; Gervais, C.; Rousse, G.; Portehault, D. Electron Precise Sodium Carbaboride Nanocrystals from Molten Salts: Single Sources to Boron Carbides. **2021**, *60*, 4252. https://doi.org/10.1021/acs.inorgchem.0c03501.

(31) Le Godec, Y.; Le Floch, S. Recent Developments of High-Pressure Spark Plasma Sintering: An Overview of Current Applications, Challenges and Future Directions. *Materials*. MDPI February 1, 2023. https://doi.org/10.3390/ma16030997.

(32) Yung, D. L.; Cygan, S.; Antonov, M.; Jaworska, L.; Hussainova, I. Ultra High-Pressure Spark Plasma Sintered ZrC-Mo and ZrC-TiC Composites. *Int. J. Refract. Met. Hard Mater.* **2016**, *61*, 201–206. https://doi.org/10.1016/j.ijrmhm.2016.09.014.

(33) Cottrino, S.; Gaudisson, T.; Pailhès, S.; Ferrara, E. A.; Mishra, S.; Daniele, S.; Mézouar, M.; Largeteau, A.; Le Godec, Y.; Le Floch, S. In Situ X-Ray Diffraction Study of a TiO2 Nanopowder Spark Plasma Sintering under Very High Pressure. *J. Eur. Ceram. Soc.* **2023**, *43* (7), 2783–2793. https://doi.org/10.1016/j.jeurceramsoc.2022.11.037.

(34) Chakraborti, A.; Jay, A.; Hardouin Duparc, O.; Sjakste, J.; Béneut, K.; Vast, N.; Le Godec, Y. Boron Carbide under Torsional Deformation: Evidence of the Formation of Chain Vacancies in the Plastic Regime. *Acta Mater.* **2022**, *226*. https://doi.org/10.1016/j.actamat.2021.117553.

(35) Jay, A.; Hardouin Duparc, O.; Sjakste, J.; Vast, N. Theoretical Raman Spectrum of Boron Carbide B4.3C under Pressure. *Acta Mater.* **2023**, *255*. https://doi.org/10.1016/j.actamat.2023.119085.

(36) Pallier, C.; Leyssale, J. M.; Truflandier, L. A.; Bui, A. T.; Weisbecker, P.; Gervais, C.; Fischer, H. E.; Sirotti, F.; Teyssandier, F.; Chollon, G. Structure of an Amorphous Boron Carbide Film: An Experimental and Computational Approach. *Chem. Mater.* **2013**, *25* (13), 2618–2629. https://doi.org/10.1021/cm400847t.

(37) Le Godec, Y.; Le Floch, S.; Pailhes, S.; Combes, J.-M. Device for Sintering by Pulsating Current and Associated Method. U.S. Patent No. 11,247,267., 2022.

(38) Léna Roumiguier. Frittage par Spark Plasma Sintering de céramiques de carbure de bore. Université de Limoges. 2019.

(39) Liu, L.; Li, X.; He, Q.; Xu, L.; Cao, X.; Peng, X.; Meng, C.; Wang, W.; Zhu, W.; Wang, Y. Sintering Dense Boron Carbide without Grain Growth under High Pressure. *J. Am. Ceram. Soc.* **2018**, *101* (3), 1289–1297. https://doi.org/10.1111/JACE.15282.

(40) Verchère, A.; Cottrino, S.; Fantozzi, G.; Mishra, S.; Gaudisson, T.; Blanchard, N.; Pailhès, S.; Daniele, S.; Floch, S. Le. Effect of High Pressure Spark Plasma Sintering on the Densification of a Nb-Doped TiO2 Nanopowder. *Ceramics* **2020**, *3* (4), 507–520. https://doi.org/10.3390/ceramics3040041.

(41) Williamson, G. K.; Hall, W. H. X-Ray Line Broadening from Filed Aluminium and Wolfram. *Acta Metall.* **1953**, *1* (1), 22–31.

(42) Brazhkin, V.; Dubrovinskaia, N.; Nicol, M.; Novikov, N.; Riedel, R.; Solozhenko, V.; Zhao, Y. What Does "harder than Diamond" Mean? *Nat. Mater.* **2004**, *3* (9), 576–577. https://doi.org/10.1055/a-0970-7610.

(43) ASTM Standard, "C1327, Standard Test Method for Vickers Indentation Hardness of Advanced Ceramics"; ASTM International, West Conshohocken, PA, 2008.

(44) Moshtaghioun, B. M.; Gomez-Garcia, D.; Dominguez-Rodriguez, A.; Todd, R. I. Grain Size Dependence of Hardness and Fracture Toughness in Pure near Fully-Dense Boron Carbide Ceramics. *J. Eur. Ceram. Soc.* **2016**, *36* (7), 1829–1834. https://doi.org/10.1016/j.jeurceramsoc.2016.01.017.

(45) Cheng, C.; Reddy, K. M.; Hirata, A.; Fujita, T.; Chen, M. Structure and Mechanical Properties of Boron-Rich Boron Carbides. *J. Eur. Ceram. Soc.* **2017**, *37* (15), 4514–4523. https://doi.org/10.1016/j.jeurceramsoc.2017.06.017.

(46) Domnich, V.; Gogotsi, Y.; Trenary, M.; Tanaka, T. Nanoindentation and Raman Spectroscopy Studies of Boron Carbide Single Crystals. *Appl. Phys. Lett.* **2002**, *81* (20), 3783. https://doi.org/10.1063/1.1521580.

(47) Farbaniec, L.; Hogan, J.; McCauley, J.; Ramesh, K. Anisotropy of Mechanical Properties in a Hot-Pressed Boron Carbide. *Int. J. Appl. Ceram. Technol.* **2016**, *13* (6), 1008–1016. https://doi.org/10.1111/IJAC.12585.

(48) Madhav Reddy, K.; Guo, J. J.; Shinoda, Y.; Fujita, T.; Hirata, A.; Singh, J. P.; McCauley, J. W.; Chen, M. W. Enhanced Mechanical Properties of Nanocrystalline Boron Carbide by Nanoporosity and Interface Phases. *Nat. Commun.* **2012**, *3*, 1–7. https://doi.org/10.1038/ncomms2047.

(49) Solozhenko, V. L.; Kurakevych, O. O.; Le Godec, Y. Creation of Nanostuctures by Extreme Conditions: High-Pressure Synthesis of Ultrahard Nanocrystalline Cubic Boron Nitride. *Adv. Mater.* **2012**, *24* (12), 1540–1544. https://doi.org/10.1002/adma.201104361.

(50) Irifune, T.; Kurio, A.; Sakamoto, S.; Inoue, T.; Sumiya, H. Ultrahard Polycrystalline Diamond from Graphite. *Nature* **2003**, *421*, 599–600. https://doi.org/10.1038/421599a.

(51) Reddy, K. M.; Liu, P.; Hirata, A.; Fujita, T.; Chen, M. W. Atomic Structure of Amorphous Shear Bands in Boron Carbide. *Nat. Commun.* **2013**, *4*, 1–5. https://doi.org/10.1038/ncomms3483.

(52) Tunistra, F.; Koenig, J. L. Raman Spectrum of Graphite. *J. Chem. Phys.* **1970**, *53* (3), 1126–1130. https://doi.org/10.1063/1.1674108.

(53) Portehault, D.; Gómez-Recio, I.; Baron, M.; Musumeci, V.; Aymonier, C.; Rouchon, V.; Le Godec, Y. Geoinspired Syntheses of Materials and Nanomaterials. *ChemicalSocietyReviews* **2022**, *51* (11), 4828–4866. https://doi.org/10.1039/D0CS01283Aï.

(54) Godec, Y. Le; Dove, M. T.; Redfern, S. A. T.; Tucker, M. G.; Marshall, W. G.; Syfosse, G.; Besson, J.-M. A New High P-T Cell for Neutron Diffraction up to 7 GPa and 2000 K with Measurement of Temperature by Neutron Radiography. *High Press. Res.* **2007**, *21* (5), 263–280. https://doi.org/10.1080/08957950108201027.

(55) Besson, J. M.; Nelmes, R. J. New Developments in Neutron-Scattering Methods under High Pressure with the Paris—Edinburgh Cells. *Phys. B Condens. Matter* **1995**, *213*, 31–36.

(56) Hammersley, A. P.; Svensson, S. O.; Hanfland, M.; Fitch, A. N.; Häusermann, D. Two-Dimensional Detector Software: From Real Detector to Idealised Image or Two-Theta Scan. *High Press. Res.* **1996**, *14* (4), 235.

(57) A. Le Bail , H. Duroy, J. L. F. Ab-Initio Structure Determination of LiSbWO6 by X-Ray Powder Diffraction. *Mat. Res. Bull.* **1988**, *23* (3), 447–452.

(58) Rodriguez-Carvajal, J. FULLPROF: A Program for Rietveld Refinement and Pattern Matching Analysis. *Abstracts of the Satellite Meeting on Powder Diffraction of the XV Congress of the IUCr*. Toulouse, France 1990, p 127.

(59) Giannozzi, P.; Baroni, S.; Bonini, N.; Calandra, M.; Car, R.; Cavazzoni, C.; Ceresoli, D.; Chiarotti, G. L.; Cococcioni, M.; Dabo, I.; et al. QUANTUM ESPRESSO: A Modular and Open-Source Software Project for Quantum Simulations of Materials. *J. Phys. Condens. Matter* **2009**, *21* (39), 395502. https://doi.org/10.1088/0953-8984/21/39/395502.

(60) Perdew, J. P.; Burke, K.; Ernzerhof, M. Generalized Gradient Approximation Made Simple. *Phys. Rev. Lett.* **1996**, *77*, 3865–3868.

(61) Troullier, N.; Martins, J. L. Efficient Pseudopotentials for Plane-Wave Calculations. *Phys. Rev. B* **1991**, *43*, 1993–2006.

(62) Kleinman, L.; Bylander, D. Efficacious Form for Model Pseudopotentials. *Phys. Rev. Lett.* **1982**, *48*, 1425.

(63) Pickard, C.; Mauri, F. All-Electron Magnetic Response with Pseudopotentials: NMR Chemical Shifts. *Phys. Rev. B* **2001**, *63*, 245101.

(64) Baxter, E. F.; Bennett, T. D.; Mellot-Draznieks, C.; Gervais, C.; Blanc, F.; Cheetham, A. K. Combined Experimental and Computational NMR Study of Crystalline and Amorphous

Zeolitic Imidazolate Frameworks. *Phys. Chem. Chem. Phys.* **2015**, *17* (38), 25191–25196. https://doi.org/10.1039/c5cp02552d.

(65) Pyykkö, P. Year-2008 Nuclear Quadrupole Moments. *Mol. Phys.* **2008**, *106*, 1965–1974.

(66) Massiot, D.; Fayon, F.; Capron, M.; King, I.; Le Calvé, S.; Alonso, B.; Durand, J. O.; Bujoli, B.; Gan, Z.; Hoatson, G. Modelling One- and Two-Dimensional Solid-State NMR Spectra. *Magn. Reson. Chem.* **2002**, *40* (1), 70–76. https://doi.org/10.1002/mrc.984.

(67) Quinn, G. D.; Bradt, R. C. On the Vickers Indentation Fracture Toughness Test. *J. Am. Ceram. Soc.* **2007**, *90* (3), 673–680. https://doi.org/10.1111/J.1551-2916.2006.01482.X.

(68) Bernard, S.; Beyssac, O.; Benzerara, K. Raman Mapping Using Advanced Line-Scanning Systems: Geological Applications. *Appl. Spectrosc.* **2008**, *62* (11), 1180–1188.

**Table of content graphic**

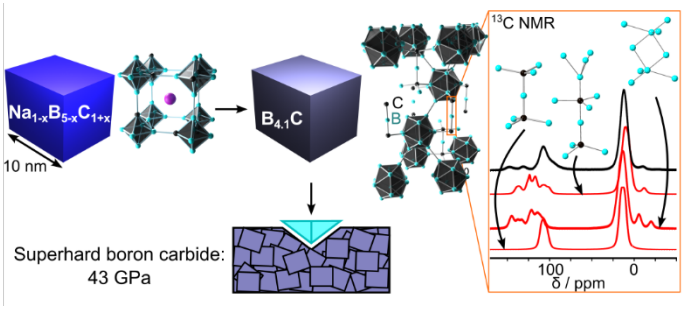

## Supporting Information

# Transforming Nanocrystals into Superhard Boron Carbide Nanostructures

Fernando Igoa Saldaña, Thomas Gaudisson, Sylvie Le Floch, Benoît Baptiste, Ludovic Delbes, Virgile Malarewicz, Olivier Beyssac, Keevin Béneut, Cristina Coelho Diogo, Christel Gervais, Gwenaëlle Rousse, Karsten Rasim, Yuri Grin, Alexandre Maître, Yann Le Godec* and David Portehault*

[1] Sorbonne Université, CNRS, Laboratoire de Chimie de la Matière Condensée de Paris (CMCP), 4 place Jussieu, F-75005, Paris, France

[2] Sorbonne Université, CNRS, MNHN, IRD, Institut de Minéralogie, de Physique des Matériaux et de Cosmochimie (IMPMC), 4 place Jussieu, F-75005, Paris, France

[3] Institut Lumière Matière, Université Lyon 1-CNRS, UMR 5306, Université de Lyon, 69622 Villeurbanne, France

[4] Sorbonne Université, CNRS, FCMat Fédération de Chimie et Matériaux de Paris Centre, FR2482, Paris, France

[5] Collège de France, Sorbonne Université, Chimie du Solide et de l'Energie (CSE), 75231 Paris Cedex 05, France

[6] Max-Planck-Institut für Chemische Physik fester Stoffe, Chemische Metallkunde, 01187 Dresden, Germany

[7] Institut de Recherche sur les Céramiques (IRCER), Centre Européen de la Céramique, 87068, Limoges, France

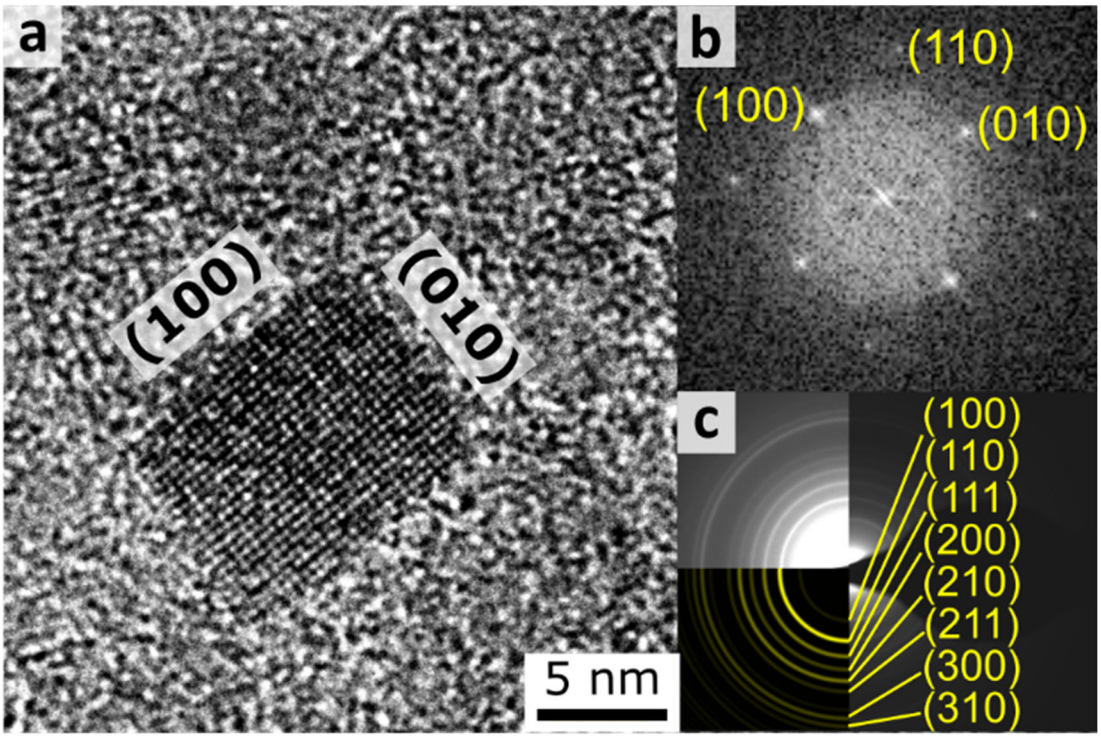


**Figure S1**. (a) High-resolution transmission electron microscopy (HRTEM) images of $Na_{1-x}B_{5-x}C_{1+x}$ sodium borocarbide nanocrystals. (b). Fast Fourier Transform (FFT) and indexation of image (a). Selected area electron diffraction (SAED) pattern fully indexed along the $NaB_5C$ structure.

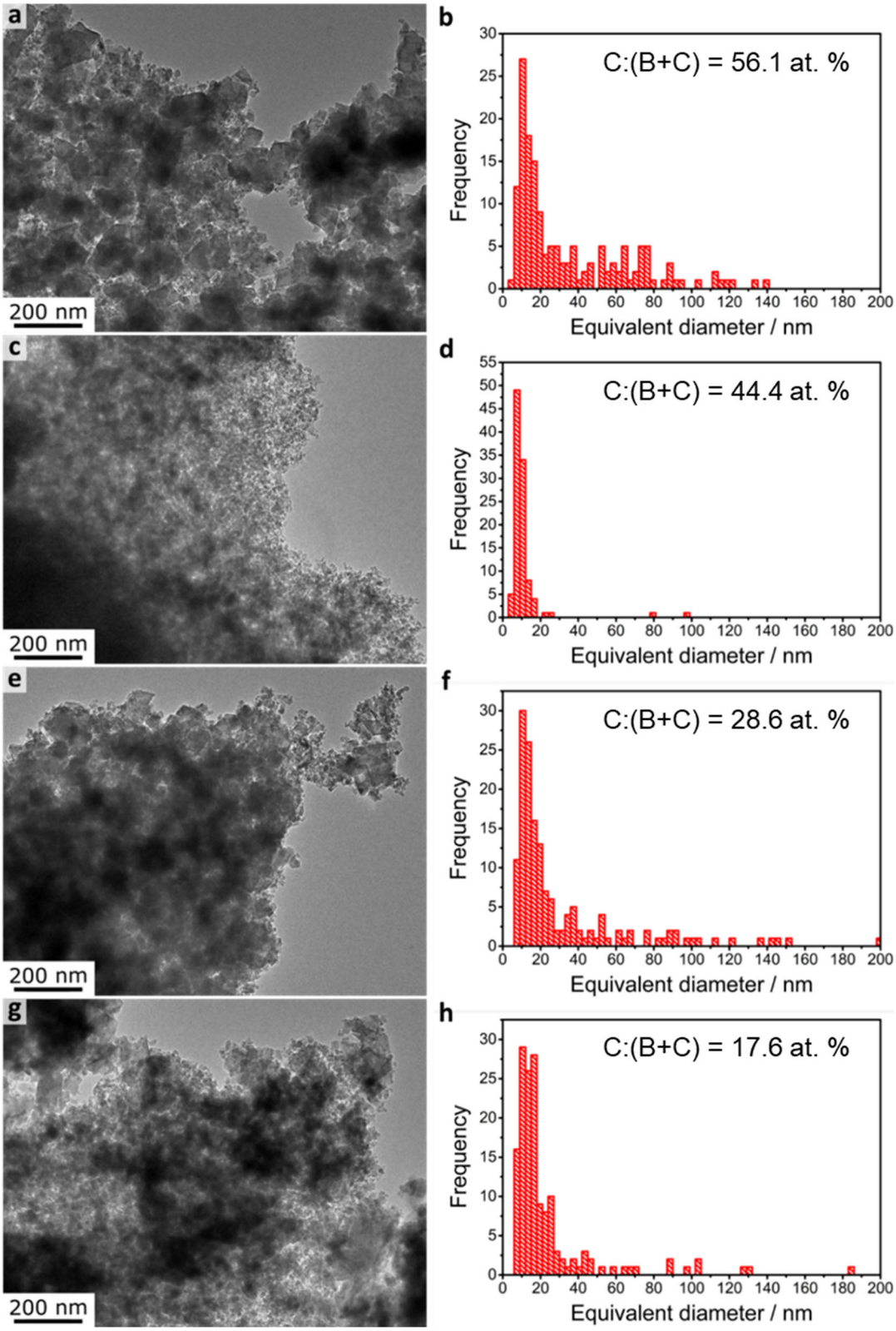


**Figure S2**. Transmission electron microscopy (TEM) images and size distribution from counting 100 particles for boron carbide samples synthesized from different C:(B+C) input ratios in the $Na_{1-x}B_{5-x}C_{1+x}$ precursor: **(a)** and **(b)** for C:(B+C) = 56.1, **(c)** and **(d)** for B:C = 44.4, **€** and **(f)** for B:C = 28.6 and **(g)** and **(h)** for B:C = 16.7 at. %.

**Table S1.** Crystallographic data of nano-$B_{4.1}C$ powder, obtained by Le Bail refinement of the structure from the X-Ray powder diffraction data at room temperature.

| **Space group** | $R\bar{3}m$ |
|---|---|
| ***a, b* (Å)** | 5.6012(2) |
| ***c* (Å)** | 12.0792(3) |
| ***α, β* (°)** | 90 |
| ***γ* (°)** | 120 |
| **Volume (Å$^3$)** | 328.185(4) |
| **Crystallite size (nm)** | 10 |
| **$R_{wp}$ (%)** | 12.6 |
| **$\chi^2$** | 5.26 |

**Table S2.** Summary of reported synthesis procedures towards boron carbide and the particle sizes attainable.

| **Reagents** | **Reaction temperature** | **Product size (dispersion)** | **Ref.** |
|---|---|---|---|
| $Na_{1-x}B_{5-x}C_{1+x}$ | 1200 °C | (10 ± 2) nm | This work |
| B(am) + Li + $CCl_4$ | 600 °C | (60 ± 30) nm | [1] |
| $B(OH)_3$ + $(CH_2CHOH)_n$ | 1400 °C | (67 ± 20) nm | [2] |
| $B(OH)_3$ + phenyl resin | 1270 °C | (70 ± 30) nm | [3] |
| $B_2O_3$ + C | 1400-1600 °C | (70 ± 50) nm | [4] |
| $B(OH)_3$ + $(CH_2CHOH)_n$ | 1600 °C | (87 ± 30) nm | [2] |
| $H_3BO_3$ + Mg + C | 750 °C | (90 ± 50) nm | [5] |

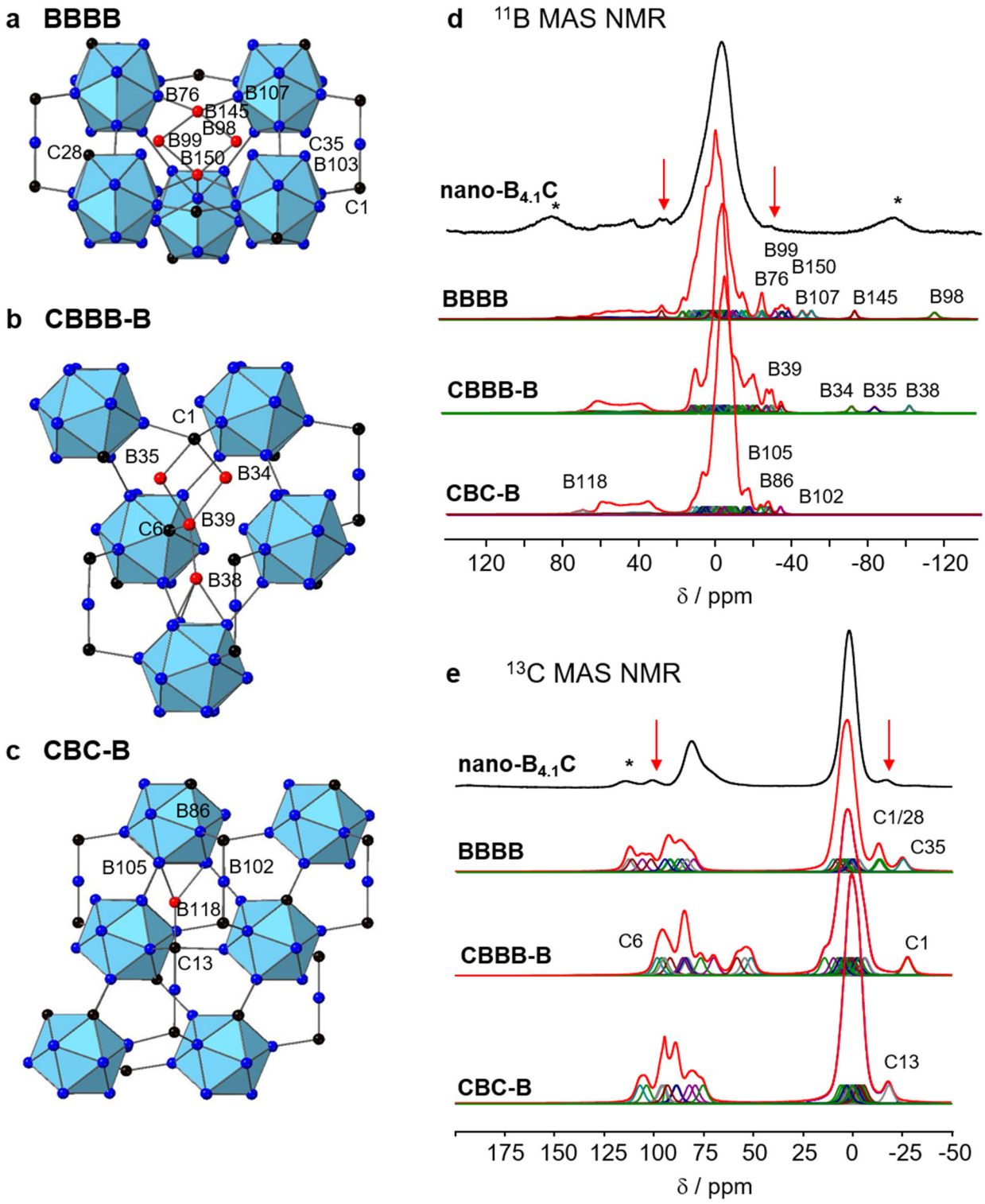


**Figure S3**. SS-NMR assignment for Nano-$B_{4.1}C$. Model structures are depicted for the **(a)** BBBB (referenced BBcBcB in ref [6], also displayed in **Figure 5**), **(b)** CBBB-B (referenced CBcBcB-Ba in ref [6] and **(c)** CBC-B (referenced CBC-Ba in ref [6], also displayed in **Figure 5**) models. Corresponding experimental and calculated $^{11}B$ and $^{13}C$ SS-NMR spectra are displayed in (**d**) and (**e**), respectively. Additional signals not ascribed to the average structure are marked with red arrows and spinning side bands with an *.

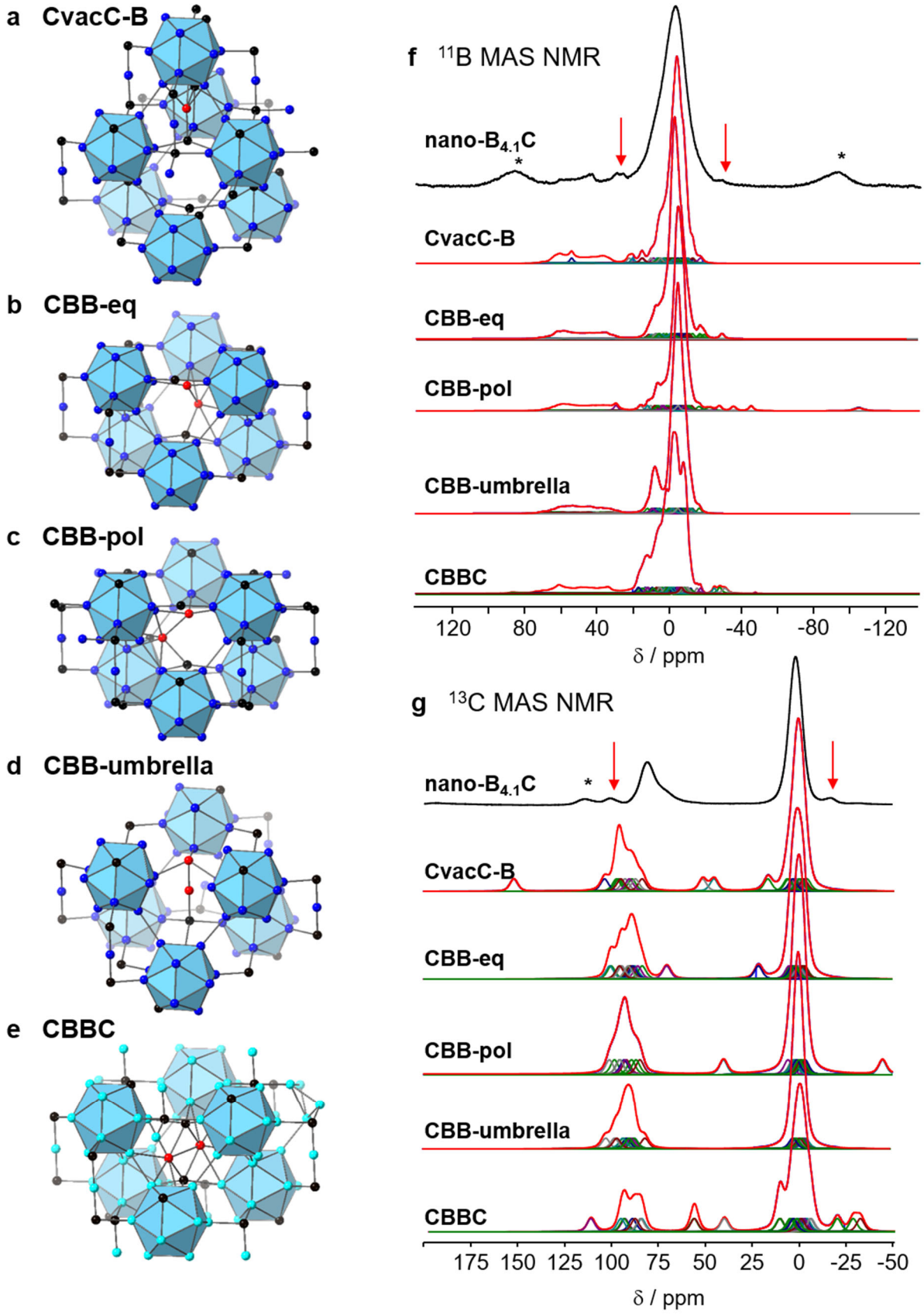


**Figure S4**. SS-NMR of Nano-$B_{4.1}C$: **(a-e)** structural models of some defects predicted with low energy.[6] Corresponding experimental and calculated $^{11}B$ and $^{13}C$ SS-NMR spectra are displayed in (**f**) and (**g**), respectively. Additional signals not ascribed to the average structure are marked with red arrows and spinning side bands with an *.

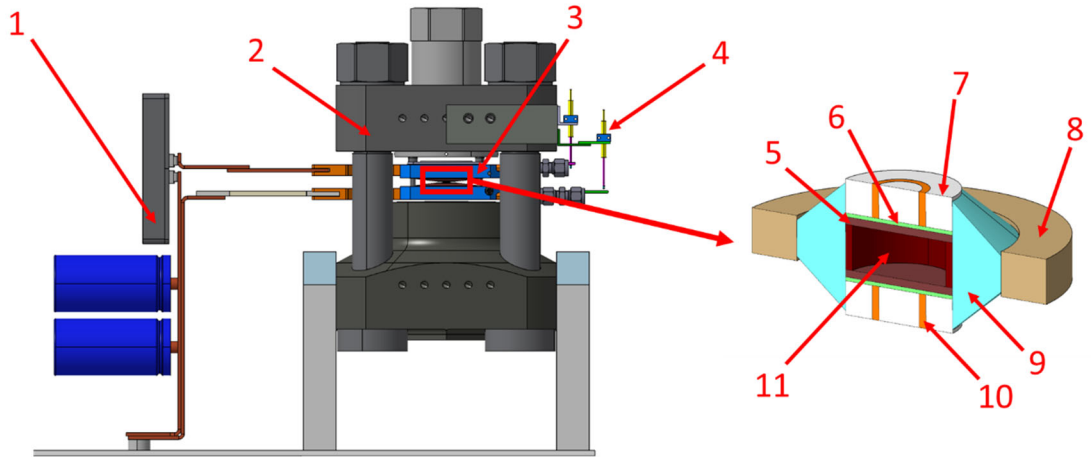


**Figure S5**. The custom-made tabletop High Pressure-Spark Plasma Sintering device. (1) Pulse generator; (2) Paris-Edinburgh press; (3) Tungsten Carbide anvils; (4) Displacement sensors; (5) Graphite mold; (6) Molybdenum foil; (7) Insulating ceramic; (8) Backup ring; (9) Pyrophyllite gasket; (10) Electrical contact; (11) Sample to densify.

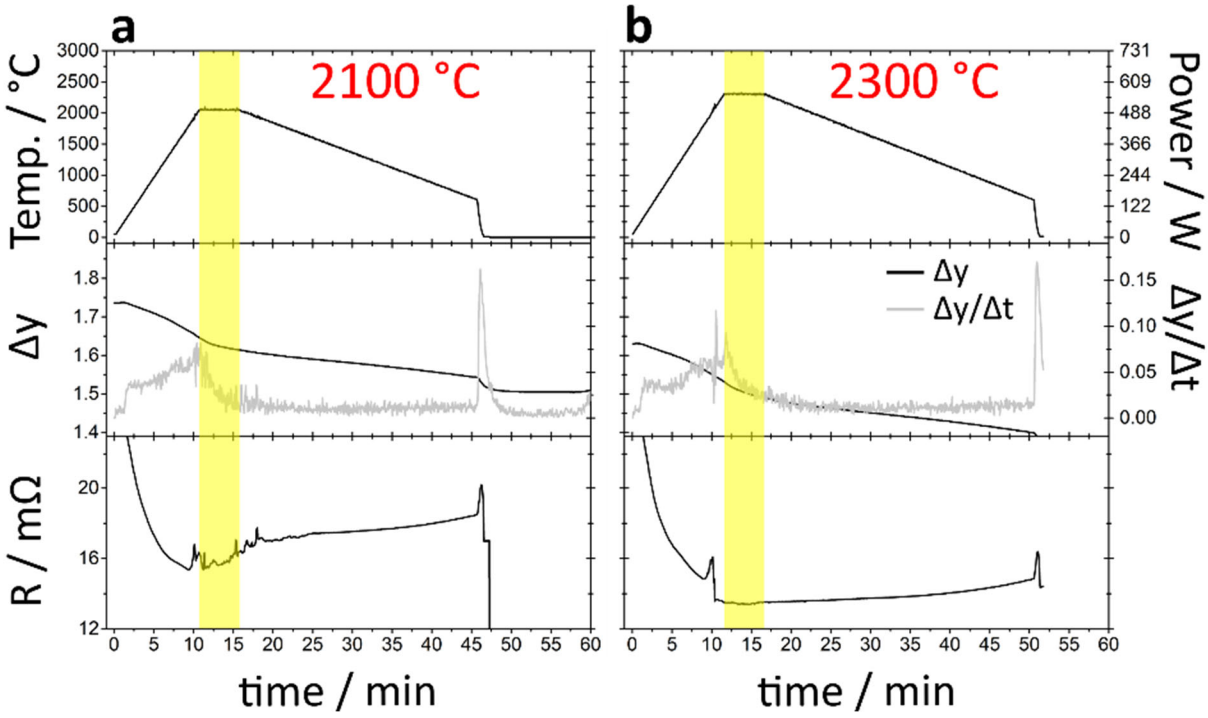


**Figure S6**. Experimental heating profile (temperature or power vs. time), displacement and displacement derivative of the anvils position over time and resistance over time for the two sintering experiments performed at 5 GPa and **(a)** 2100 °C or **(b)** 2300 °C.

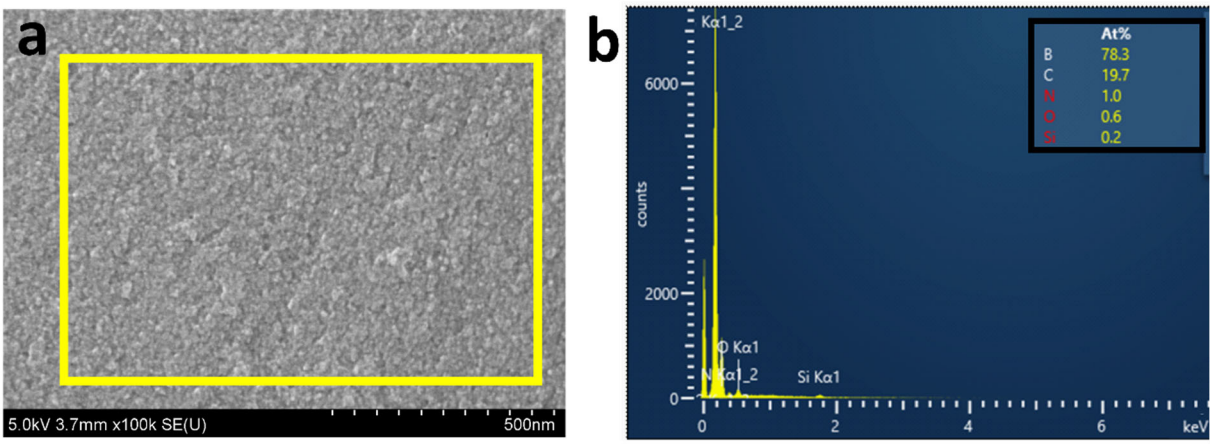


**Figure S7**. SEM image from the **nano-$B_{4.1}C$-2300** sample **(a)**. EDS spectrum from marked region in **(a)**, showing the absence of Na in the final product **(b)**.

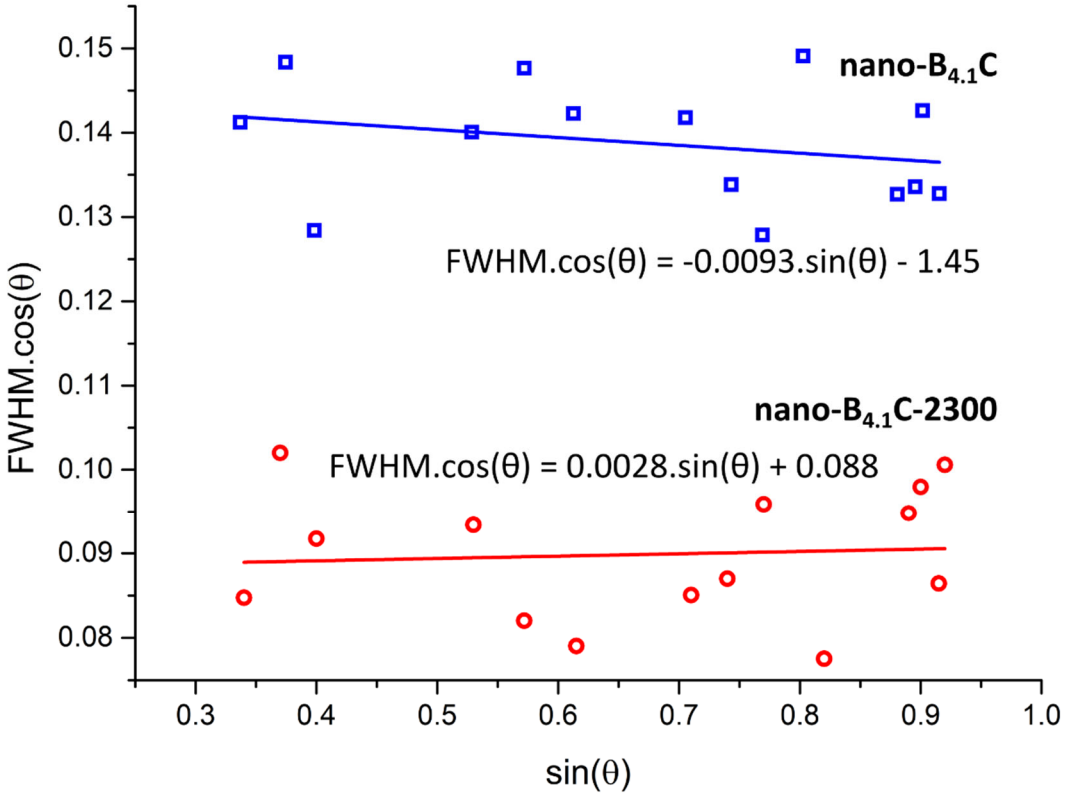


**Figure S8**. Williamson-Hall plots for the as-prepared **nano-$B_{4.1}C$** and the sintered **nano-$B_{4.1}C$-2300** samples. The strain is proportional to the slope, which is close to null in both cases.

**Table S3.** Crystallographic data of nano-$B_{4.1}C$ monolith sintered at 2100 °C (nano-$B_{4.1}C$-2100), obtained by Le Bail refinement of the structure from the X-Ray powder diffraction data at room temperature.

| **Space group** | $R\bar{3}m$ |
|---|---|
| ***a, b* (Å)** | 5.6050(3) |
| ***c* (Å)** | 12.0811(3) |
| ***α, β* (°)** | 90 |
| ***γ* (°)** | 120 |
| **Volume (Å$^3$)** | 328.682(2) |
| **Crystallite size (nm)** | 16 |
| **$R_{wp}$ (%)** | 4.67 |
| **$\chi^2$** | 3.15 |

**Table S4.** Crystallographic data of nano-$B_{4.1}C$ monolith sintered at 2300 °C (nano-$B_{4.1}C$-2300), obtained by Le Bail refinement of the structure from the X-Ray powder diffraction data at room temperature.

| **Space group** | $R\bar{3}m$ |
|---|---|
| ***a, b* (Å)** | 5.5996(2) |
| ***c* (Å)** | 12.0799(3) |
| ***α, β* (°)** | 90 |
| ***γ* (°)** | 120 |
| **Volume (Å$^3$)** | 328.016(3) |
| **Crystallite size (nm)** | 21 |
| **$R_{wp}$ (%)** | 6.63 |
| **$\chi^2$** | 2.69 |

## References


(1) Gu, Y.; Chen, L.; Qian, Y.; Zhang, W.; Ma, J. Synthesis of Nanocrystalline Boron Carbide via a Solvothermal Reduction of CCl4 in the Presence of Amorphous Boron Powder. *J. Am. Ceram. Soc.* **2005**, *88* (1), 225–227. https://doi.org/10.1111/j.1551-2916.2004.00023.x.

(2) Fathi, A.; Ehsani, N.; Rashidzadeh, M.; Baharvandi, H.; Rahimnejad, A. Synthesis of Boron Carbide Nano Particles Using Polyvinyl Alcohol and Boric Acid. *Ceram. - Silikaty* **2012**, *56* (1), 32–35.

(3) Najafi, A.; Golestani-Fard, F.; Rezaie, H. R.; Ehsani, N. A Novel Route to Obtain B 4C

Nano Powder via Sol-Gel Method. *Ceram. Int.* **2012**, *38* (5), 3583–3589. https://doi.org/10.1016/j.ceramint.2011.12.074.
(4) Herth, S.; Joost, W. J.; Doremus, R. H.; Siegel, R. W. New Approach to the Synthesis of Nanocrystalline Boron Carbide. *J. Nanosci. Nanotechnol.* **2006**, *6* (4), 954–959. https://doi.org/10.1166/jnn.2006.186.
(5) Farzaneh, F.; Golestanifard, F.; Sheikhaleslami, M. S.; Nourbakhsh, A. A. New Route for Preparing Nanosized Boron Carbide Powder via Magnesiothermic Reduction Using Mesoporous Carbon. *Ceram. Int.* **2015**, *41* (10), 13658–13662. https://doi.org/10.1016/j.ceramint.2015.07.163.
(6) Rasim, K.; Ramlau, R.; Leithe-Jasper, A.; Mori, T.; Burkhardt, U.; Borrmann, H.; Schnelle, W.; Carbogno, C.; Scheffler, M.; Grin, Y. Local Atomic Arrangements and Band Structure of Boron Carbide. *Angew. Chemie Int. Ed.* **2018**, *130* (21), 6238–6243. https://doi.org/10.1002/anie.201800804.